



HAL
open science

Multiscale investigation of cement pastes with low and high-grade calcined clays and slag at early and advanced ages

Imane Bekrine, Benoit Hilloulin, Ahmed Loukili

► To cite this version:

Imane Bekrine, Benoit Hilloulin, Ahmed Loukili. Multiscale investigation of cement pastes with low and high-grade calcined clays and slag at early and advanced ages. *Journal of Building Engineering*, 2023, pp.107570. 10.1016/j.jobbe.2023.107570 . hal-04187611

HAL Id: hal-04187611

<https://hal.science/hal-04187611v1>

Submitted on 25 Aug 2023

HAL is a multi-disciplinary open access archive for the deposit and dissemination of scientific research documents, whether they are published or not. The documents may come from teaching and research institutions in France or abroad, or from public or private research centers.

L'archive ouverte pluridisciplinaire **HAL**, est destinée au dépôt et à la diffusion de documents scientifiques de niveau recherche, publiés ou non, émanant des établissements d'enseignement et de recherche français ou étrangers, des laboratoires publics ou privés.

Multiscale investigation of cement pastes with low and high-grade calcined clays and slag at early and advanced ages

I. Bekrine¹, B. Hilloulin¹, A. Loukili¹

Nantes Université, Ecole Centrale Nantes, CNRS, Institut de Recherche en Génie Civil et Mécanique (GeM), UMR 6183, F-44000
Nantes, France

ABSTRACT

Clays are abundant materials worldwide, but the massive demand for pure kaolinitic clays in multiple fields could reduce the availability of high-grade calcined clay. For this reason, the properties of cementitious materials with low-grade calcined clays should be seriously investigated. In this work, binary and ternary binders composed of high-grade or low-grade calcined clays and slag, replacing 30% of Portland cement, are studied using nanoindentation, standard strength measurement, MIP, and SEM in order to demonstrate the impact of calcined clay composition on the microscale and macroscale properties of cementitious materials during both early and mature ages. Results show that in binary binders, low-grade calcined clay leads to reduced porosity and enhanced elastic and viscoelastic properties, as probed by means of nanoindentation, while high-grade calcined clay results in a high amount of low-density calcium silicate hydrate (LD CSH). Moreover, in the ternary binder, a synergistic effect has been highlighted between low-grade calcined clay and slag through the improvement of compressive strength at early age, as well as a refinement of the pore structure. From this study, it can be concluded that low-grade calcined clays give rise to good micromechanical properties and can be particularly effective in ternary blends when associated with slag.

Keywords: Nanoindentation, Micromechanical Properties, Creep, Microstructure, Calcined Clay, Blast Furnace Slag.

31 **Summary of abbreviations**

Mineral additions

SCMs Supplementary cementitious materials

CC Calcined clay

GBFS Granulated blast furnace slag

Pastes' phases

LD CSH Low-density CSH

HD CSH High-density CSH

CH Portlandite/calcium hydroxide

UC Unhydrated cement

Q Quartz

M Muscovite

Atomic species

Al Aluminium

K Potassium

Ca Calcium

Si Silicon

Experimental and numerical techniques

XRD X-ray diffraction

SEM Scanning electron microscope

EDS Energy dispersive spectroscopy

BSE Backscattered electrons

MIP Mercury intrusion porosity

TGA Thermogravimetric analysis

GMM Gaussian Mixture Model

32 **1. Introduction**

33 Cement production is a highly CO₂-emitting process. Its main constituent, clinker, is obtained by
34 limestone and natural clays being fired at 1,450°C, which requires fossil fuels for heating and induces
35 limestone decarbonation. To reduce this substantial environmental impact, supplementary
36 cementitious materials (SCMs) can partially replace cement in concrete. Commonly used SCMs
37 include fly ash, silica fume and granulated blast furnace slag; however, these are only available in
38 limited supplies. Fine limestone and natural pozzolans are also employed, but their reactivity remains
39 low when used alone. The introduction of calcined clays in cement blends has thus received great

40 attention of late due to their smaller carbon footprint, widespread availability [1] and potential to
41 improve cementitious material properties.

42 Replacing a portion of Portland cement with calcined clays results in several changes in the cement
43 paste hydration products. In addition to calcium-silicate-hydrate (CSH), calcium hydroxide (CH) and
44 ettringite, which are the main hydration products of a Portland cement paste, other products may be
45 formed depending on the raw clay composition. For instance, the alumina-rich amorphous phase of
46 metakaolin (MK) triggers the formation of calcium aluminosilicate hydrates (CASH), CAH,
47 strätlingite C_2ASH_8 , and hydrogranet C_3AH_6 or C_4AH_{13} , depending on both the AS_2/CH ratio (AS_2
48 stands for $Al_2O_3 \cdot 2SiO_2$) and reaction temperature [2]. In the presence of reactive calcite, calcium
49 hemicarboaluminate hydrates (Hc) are also formed as a consequence of ettringite conversion [3]. The
50 hydration kinetics are also modified with calcined clay incorporation, since they accelerate the
51 hydration of clinker minerals, with ettringite being formed faster [4], which also increases the heat of
52 hydration, as reported in [5]. Moreover, calcined clays are pozzolanic materials, which results in
53 calcium hydroxide consumption inside the cement paste after several days/weeks [6].

54 Overall, it has been proven that incorporating calcined clays is beneficial to cementitious materials,
55 as regards the majority of their properties. It has also been shown that compressive strength increases
56 relative to pure cement reference samples, especially at early ages, given that the filler effect is
57 immediate [7], as is the elastic modulus [8,9]. Durability properties may actually be enhanced with
58 calcined clay incorporation through pore size refinement [10]. In their study, Dwivedi *et al.* pointed
59 out that a 20% replacement of cement by metakaolin in mortars reduces the number of capillary pores,
60 thus leading to decreased permeability [11]. Chloride ion ingress is also reduced [12,13], as is the
61 resistance to freeze-thaw cycles [14].

62 However, the use of calcined clays in cementitious systems also has some drawbacks, such as a loss
63 of workability due to its high specific surface area [15]. The use of other SCMs with calcined clays
64 can serve to overcome these obstacles and enhance other properties. Recently, several studies have
65 demonstrated the efficiency of using calcined clays with limestone in LC^3 binders, in improving
66 chloride resistance [16,17] and preventing the alkali-silica reaction [18]. Similarly, the use of calcined
67 clays with slag improves fluidity of the cement blend [19] as well as compressive strength [20]. Even
68 though several works have studied the hydration and macromechanical properties of calcined clay-
69 based cementitious blends, their micromechanical properties are rarely addressed, especially at an
70 early age. In addition, the effect of the calcined clay grade on several properties of cementitious
71 materials was studied, such as rheology [21], hydration and mechanical performance [22–24],

72 printability [25], but there is no such study to determine its effect on micromechanical properties,
73 namely elastic modulus, hardness, and contact creep modulus, of the cementitious materials phases,
74 which is of huge importance to understand the observed behaviors at the macroscale.

75 Microindentation and nanoindentation were applied as local mechanical investigation techniques in
76 order to assess the mechanical properties of cementitious materials [26]. Some studies used these
77 techniques to investigate localized phenomena, such as the interfacial transition zone (ITZ) [27,28]
78 and carbonated areas [29], while others targeted specific phases of interest in a heterogeneous material
79 [30]. Nonetheless, since cementitious materials exhibit heterogeneous features, the majority of studies
80 performed a large number of indentations in the regular grid forms so as to study the cement pastes;
81 the properties of the various phases were determined by means of different clustering methods,
82 namely least-square estimation (LSE) and maximum likelihood estimation (MLE) [31–33]. A number
83 of studies on pure cement mixes were conducted according to these techniques [34–36], then
84 extending to mixes containing SCMs to assess their effect on micromechanical properties. The elastic
85 modulus of the CSH phase was indeed found to be 10% lower when silica fume and fly ash were
86 incorporated [37], while another study demonstrated that the elastic properties did not change with
87 fly ash incorporation [38]. Instead, the fractions of portlandite decreased and those of high-density
88 CSH increased [37,38], which was explained by the pozzolanic reaction. Evidence of the pozzolanic
89 reaction has also been proven in the presence of metakaolin [39] and slag [40]. The incorporation of
90 pure metakaolin (96.4% amorphous phase) and slag resulted in an increase of CSH porosity at 7 days
91 [41].

92 Over the last two decades, a study of the viscoelastic behavior of materials subjected to
93 microindentation and nanoindentation techniques has been added as well. These techniques have
94 speeded the characterization of creep properties of cementitious materials by applying a constant load
95 for several tens of seconds on the tested materials; in contrast, measuring creep properties typically
96 takes weeks to years at the scale of concrete laboratory samples or actual structures [42,43]. Although
97 the creep mechanism of cementitious materials has yet to be well understood, it is generally agreed
98 that CSH acts as the primary cause. In [44,45], the authors proved that CSH exhibits logarithmic
99 creep properties that depend solely on CSH packing density. Several studies were subsequently
100 conducted to investigate the creep properties of cementitious materials [43-45]. Li and colleagues
101 have examined the effect of various cement paste phases on cement paste creep properties and
102 underscored the importance of considering the actual pore creep modulus instead of 0 GPa, as well
103 as the possibility of considering all unhydrated particles, despite a wide range of creep property
104 variation, as a single phase in homogenization schemes [49]. The impact of SCMs on viscoelastic

105 properties has rarely been assessed although they may play a significant role in the modern green
106 concrete creep phenomenon. Li *et al.* have shown that a 10% cement replacement with silica fume
107 was found to enhance the CSH creep modulus [50]; but to the best of the authors' knowledge, no such
108 studies on calcined clay binary or ternary blends have yet to be conducted, especially at an early age.

109 In this study, the micromechanical properties of binary and ternary calcined clay-blended pastes at
110 both early and advanced ages will be investigated, and the advantage of using low-grade calcined
111 clays in terms of performance will be demonstrated, along with their availability, lower environmental
112 impact (due to lower calcination temperatures) and lower cost. To this end, a comprehensive
113 comparison of the pastes microstructure and nanoindentation-inferred micromechanical properties
114 will be drawn between low-grade and high-grade calcined clay-based cement pastes. Next, the effect
115 of slag addition on the Portland cement / low-grade calcined clay system will be discussed and the
116 synergistic effect of slag and low-grade calcined clay highlighted.

117

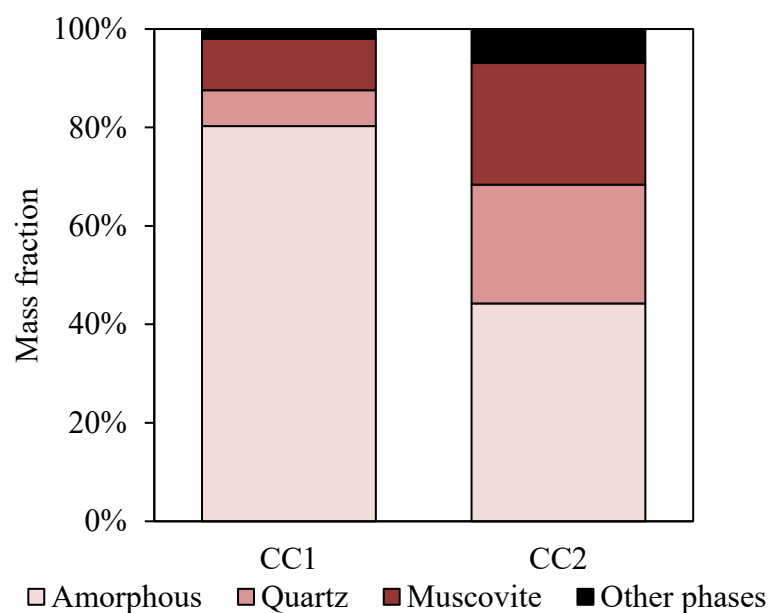
118 2. Materials and methods

119 2.1 Materials and sample preparation

120 **The materials used in this study are Portland cement CEM I 52.5 N, two distinct calcined**
121 **clays CC1 and CC2, respectively originated from “Charentes” and “Mariais” extraction sites**
122 **in France, and granulated blast furnace slag (GBFS). The chemical composition and physical**
123 **properties of the binders are given in**

124 Table 1.

125



126

127 Fig. 1 shows the mineralogical composition of the studied calcined clays obtained by means of XRD
 128 and quantified by Rietveld analysis using the external standard method. According to the figure, CC1
 129 and CC2 are mostly composed of amorphous phase (80.2% and 44.2% resp.), muscovite (10.4% and
 130 24.7% resp.) and quartz (7.3% and 24.1% resp.). Other phases were identified in minor amounts such
 131 as kaolinite, rutile, albite and mullite. In the rest of this paper, CC1 and CC2 will be respectively
 132 assigned as high-grade and low-grade calcined clays given their amorphous phase content. The
 133 impact of this difference in calcined clays composition on the micromechanical properties of cement
 134 pastes will be investigated.

135

136

137

138

139 **Table 1**

140 Chemical and physical properties of the materials used in this study

		Cement	GBFS	CC1	CC2
Chemical composition (%)	SiO ₂	20.4	37.7	53.95	62.70
	Al ₂ O ₃	4.4	10.2	38.48	27.86
	Fe ₂ O ₃	2.3	0.6	1.82	2.98
	TiO ₂	-	0.7	1.53	0.35
	CaO	64.0	43.8	0.04	0.10
	MgO	3.9	6.4	0.19	0.39
	SO ₃	2.9	0.1	-	-
	K ₂ O	0.66	0.28	1.04	2.50
	Na ₂ O	0.15	0.21	0.10	0.14
	P ₂ O ₅	0.1	-	0.07	0.08
	Cl ⁻	0.02	0.02	-	-
	S ²⁻	<0.02	0.7	-	-
	Na ₂ O eq.	0.58	0.44	-	-
Physical properties	Specific gravity (g/cm ³)	3.15	2.9	2.2	2.5
	Specific area (cm ² /g)	3979	4450	190000	160000

141

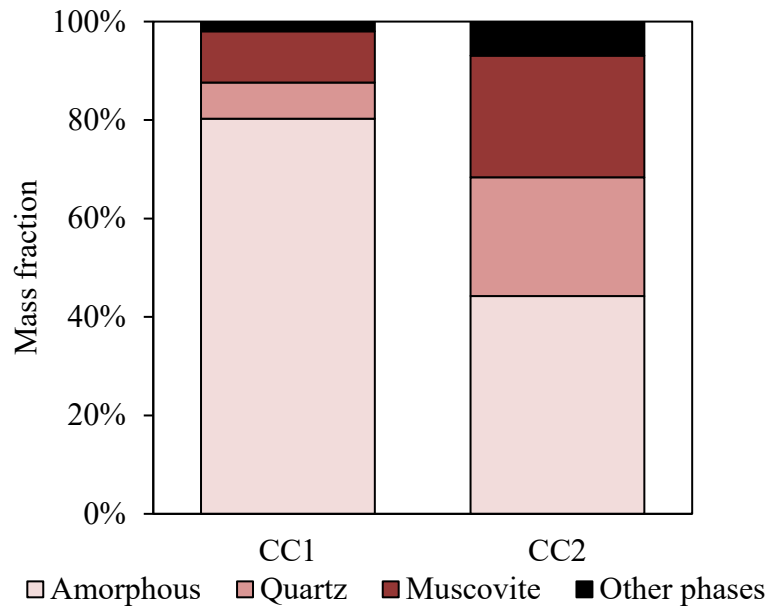


Fig. 1. Calcined clay compositions as determined using XRD/Rietveld analysis

Using these raw materials, water and superplasticizer (depending on the mix workability), four cement pastes with a constant water-to-binder ratio of 0.3 were manufactured. 30% of cement (by volume) was replaced by mineral additions in the binary and ternary binders. The binder proportions are detailed in Table 2.

Table 2

Cement paste binder compositions (volume proportions)

Paste reference	Cement (%)	GBFS (%)	CC1 (%)	CC2 (%)
P ₀	100	-	-	-
PCC1 ₃₀	70	-	30	-
PCC2 ₃₀	70	-	-	30
PCC2 ₁₅ S ₁₅	70	15	-	15

The $4 \times 4 \times 16 \text{ cm}^3$ cement paste prisms were manufactured, standard cured, demolded at 24 h and kept in lime-saturated water at 20°C until reaching testing age. Then, 1-2 cm cubes were sawn at the testing age, placed in 99.8% isopropanol for 4 days to stop hydration, and dried at 40°C for 4 other days [51]. As explained in [52], all hydration stoppage procedures were proven to cause microscopic modifications to the sample, although isopropanol is weaker and causes less damage.

For the nanoindentation and SEM tests, the cubes were impregnated in cold mounting epoxy resin. Special care was paid to the sample polishing step in order to achieve smooth surfaces: coarse

158 polishing was performed using SiC abrasive papers of decreasing grain sizes from 120 to 4000 grit
159 (corresponding resp. to 68 μm - 5.3 μm), then fine polishing using diamond pastes on woven natural
160 silk discs of 3 μm and 1 μm grain sizes. Ethanol was used as a polishing lubricant to prevent further
161 hydration. After each polishing step, the samples were cleaned in an ethanol ultrasonic bath for a few
162 minutes to remove all suspensions and debris on the surface. Surface quality was assessed by means
163 of the Scanning Probe Microscopy (SPM) mode of the nanoindenter, with the Root Mean Square
164 (RMS) roughness being calculated on $50 \times 50 \mu\text{m}^2$ surfaces.

165 2.2 Methods

166 2.2.1 Macromechanical testing

167 The compressive strength was measured on $4 \times 4 \times 16 \text{ cm}^3$ prisms previously split into two, on at
168 least four samples at 2 and 28 days according to NF EN 196-1 standard.

169 2.2.2 Thermogravimetric analysis

170 Portlandite content in the mixes was determined using TGA in order to assess the binders' pozzolanic
171 activity, according to ASTM C1872-18 standard. For this purpose, a NETZSCH microbalance was
172 used with N_2 purging gas and a rate of 60 mL/min. $50 \pm 5 \text{ mg}$ of crushed powder were placed in
173 alumina crucibles and subjected to raising temperatures from 20°C to 1000°C with a heating rate of
174 $10^\circ\text{C}/\text{min}$. The weight loss WL_{CH} (%) of portlandite due to the evaporation of water was determined
175 using the tangential method of Marsh [53] between 400°C and 550°C , and the measured mass
176 proportion mm_{CH} (%) of portlandite as well as its actual mass proportion in the sample m_{CH} (%) are
177 deduced using respectively the equations below:

$$178 \quad mm_{CH}(\%) = WL_{CH} \times \frac{M_{CH}}{M_{H_2O}} \quad (1)$$

$$179 \quad m_{CH}(\%) = \frac{mm_{CH}(\%)}{m_{600^\circ\text{C}} \times \left(1 + \frac{w}{b}\right)} \quad (2)$$

180 where $M_{CH}=74 \text{ g/mol}$ is the molar mass of portlandite, $M_{H_2O}=18 \text{ g/mol}$ is the molar mass of water,
181 $m_{600^\circ\text{C}}$ is the sample mass at 600°C and $w/b=0.3$ is the water-to-binder ratio of all cement pastes.

182 2.2.3 Mercury intrusion porosity

183 The pore structure of the various cement pastes was investigated using a Micromeritics AutoPore IV
184 mercury porosimeter according to ISO 15901-1:2016 standard. The mercury pressure gauge was used
185 at a maximum pressure of 400 MPa, which corresponds to a minimum pore radius of 1.5 nm. Each
186 cement paste mix was tested at 2 and 28 days.

187 2.2.4 Scanning electron microscopy - Energy dispersive spectroscopy (SEM/EDS)

188 Scanning electron microscopy equipped with X-ray energy dispersive spectroscopy (SEM/EDS) was
189 conducted to characterize the blended cement pastes microstructures. Backscattered electron (BSE)
190 images were captured using an accelerating voltage of 15 kV, at working distance of 17 mm and a
191 magnification of 300×. A surface scan of the chemical composition with an EDS detector was needed
192 to roughly detect the nature of certain observed phases on BSE micrographs through the resulting
193 elemental maps.

194 2.2.5 Nanoindentation

195 Nanoindentation experiments were performed using a Bruker TS 77 Berkovich nanoindenter, in order
196 to study the micromechanical properties of individual phases of the cement pastes. While in SPM
197 mode, the smoothest parts of the samples (RMS < 50 nm) were targeted in order to carry out
198 nanoindentation tests. Three grids of 20 × 20 indents, equally spaced at 5 μm, were executed using a
199 load-controlled function, with a trapezoidal loading composed of a loading phase in 5 s, a holding
200 phase of 60 s at maximum load P_{max} of 2 mN and an unloading phase of 5 s. Continuous measurements
201 of penetration depth with these applied loads were recorded at a frequency of 200 Hz; consequently,
202 the slope of the unloading curve at maximum load S could be determined.

203 The reduced elastic modulus E_r , elastic modulus E and hardness H were all then calculated as per the
204 Oliver and Pharr method [54]:

205
$$E_r = \frac{1}{2} \sqrt{\frac{\pi}{A_c}} S \quad (3)$$

206
$$\frac{1}{E_r} = \frac{1 - \nu^2}{E} + \frac{1 - \nu_{ind}^2}{E_{ind}} \quad (4)$$

207
$$H = \frac{P_{max}}{A_c} \quad (5)$$

208 where ν is the material Poisson's ratio, which equals 0.24 for cement paste [55]; $\nu_{ind} = 0.07$ and
209 $E_{ind} = 1,141$ GPa are respectively the diamond indenter Poisson's ratio and its elastic modulus. A_c
210 denotes the projected contact area between the indenter tip and the indented surface, as obtained by
211 the tip-area function calibration on a fused silica standard sample with incremental loads ranging
212 from 100 μN to 10,000 μN by 100 μN increments.

213 In order to calculate viscoelastic properties from the nanoindentation tests, the variation in penetration
 214 depth $\Delta h(t) = h(t) - h_0$, where h_0 represents the initial penetration depth, is logarithmically fitted
 215 as:

$$216 \quad \Delta h(t) = x_1 \ln(1 + x_2 t) \quad (6)$$

217 where x_1 and x_2 are the parameters to fit; they are related to the creep modulus and characteristic time
 218 respectively by the following expressions:

$$219 \quad C = \frac{P_{max}}{2a_U x_1} \quad (7)$$

$$220 \quad \tau = \frac{1}{x_2} \quad (8)$$

221 where $a_U = \sqrt{A_c/\pi}$ is the contact radius.

222 All abnormal load-depth curves [56] were deleted prior to conducting a statistical analysis of the
 223 results.

224 2.2.6 Deconvolution process

225 The analysis of each indentation curve provides information about the mechanical properties of each
 226 point k in the grid, i.e. values of elastic modulus, hardness and contact creep modulus (E_k, H_k, C_k).
 227 In this deconvolution process, the total distribution x of both elastic modulus and hardness $x = (E, H)$
 228 was assumed a mixture of individual phases, where each phase is seen as a two-dimensional Gaussian
 229 distribution. The statistical deconvolution is then performed to cluster all the data into N mixture
 230 components, i.e. N clusters. The number of clusters was chosen based on the Bayesian Information
 231 Criterion (BIC). The probability density function of the Gaussian Mixture Model (GMM) is given in
 232 equation (9), and the one for each phase is given in equation (11):

$$233 \quad p(x) = \sum_{i=1}^N \pi_i N(x|\mu_i, \Sigma_i) \quad (9)$$

$$234 \quad \sum_{i=1}^N \pi_i = 1 \quad (10)$$

$$235 \quad N(x|\mu, \Sigma) = \frac{1}{\sqrt{\det(2\pi\Sigma)}} e^{-\frac{1}{2}(x-\mu)\Sigma^{-1}(x-\mu)} \quad (11)$$

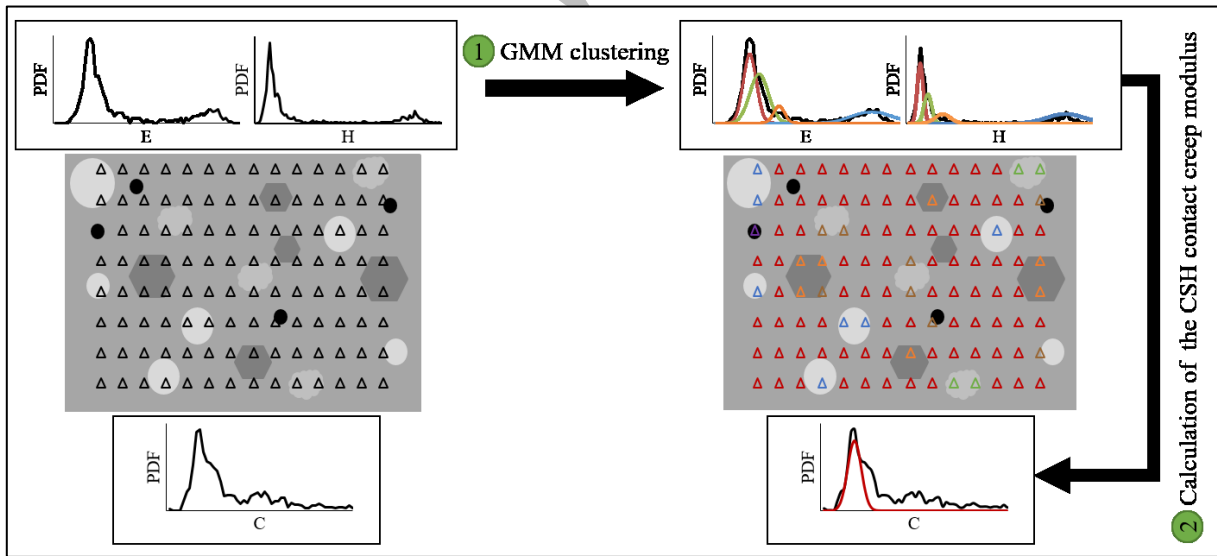
236 where π_i , μ_i and Σ_i are respectively the weighting coefficient, the mean value and the covariance of
 237 the i-th component.

238 To find the parameters (the weighting coefficient, the mean and the covariance) that maximize the
 239 joint probability, the following optimization problem is solved using Monte-Carlo search:

$$240 \quad \max(\ln(\prod_{j=1}^M p(x_j))) = \max(\sum_{j=1}^M \ln(\sum_{i=1}^N \pi_i N(x|\mu_i, \Sigma_i))) \quad (12)$$

241 where M is the number of observations, which is the number of indents.

242 To achieve this, Expectation-Maximization (EM) algorithm was used, where data were assigned to
 243 the closest randomly chosen means, the means recalculated based on the assigned data and so on until
 244 the calculated means are no more changing. Initial values were given by K-means algorithm in order
 245 to reduce the calculation time. This first step of calculation was referred to as (1) in Fig. 2 illustrating
 246 the calculation process. Finally, the mean and standard deviation of contact creep modulus on the
 247 CSH resulting clusters were calculated for all the samples, which was referred to as (2) in Fig. 2.



248

249 **Fig. 2.** Calculation process of the clusters micromechanical properties

250

251 The clusters determined by this deconvolution process do not necessarily correspond to pure phases,
 252 but the predominant ones can be determined depending on the mean and standard deviation values of
 253 E and H. In literature, the properties of the known main phases in Portland cement pastes (LD and
 254 HD CSH, portlandite, unhydrated cement) were widely reported. In addition to these known phases,

255 the values of elastic properties of some others, contained in our pastes and brought by the mineral
 256 additions, are given in Table 3 with the references from the literature. The assignment of predominant
 257 phases in each cluster starts by looking at the standard deviation: if it is high with respect to the mean
 258 value, then the cluster contains more than a predominant phase; if it is low, then the cluster is mono-
 259 phase. Then, the cluster's mean property is compared to values reported in the literature to assign
 260 suitable phase(s) to each cluster.

261 **Table 3**

262 Elastic properties of some phases in the literature (mean or mean \pm standard deviation)

Phase	E (GPa)	H (GPa)	Reference
Unhydrated slag	72.4 \pm 8.7	5.06 \pm 1.18	[40]
Quartz	77.4	10.2	[57]
Muscovite	55.6	2.7	[57]

263 **3. Results**

264 *3.1 Macroscopic compressive strength*

265 Fig. 3 compares the compressive strength of the four cementitious systems at 2 and 28 days. First, we
 266 can notice a strength-gain from 2 to 28 days in all the mixes, which is higher for the blended cement
 267 pastes compared to the reference mix, and the highest in PCC2₃₀ with 57.7% gain. At 2 days, the
 268 average compressive strength of the reference mix and PCC1₃₀ are maximum, reaching nearly
 269 60 MPa. Incorporating CC2 into the system causes a drop in compressive strength of 25.7% relative
 270 to the reference mix. This finding indicates a better mechanical performance for PCC1₃₀ at an early
 271 age. Incorporating slag with CC2 increased by 17.2% the compressive strength with respect to
 272 PCC2₃₀, which suggests a synergistic effect between the two additions. At 28 days, PCC1₃₀ developed
 273 the highest compressive strength among all cement blends. Interestingly, PCC2₃₀ developed an
 274 equivalent compressive strength to the reference mix, therefore proving the benefit of using low-
 275 grade calcined clay. It is also worth noting that small differences in strength were obtained between
 276 the ternary binder and the reference mix.

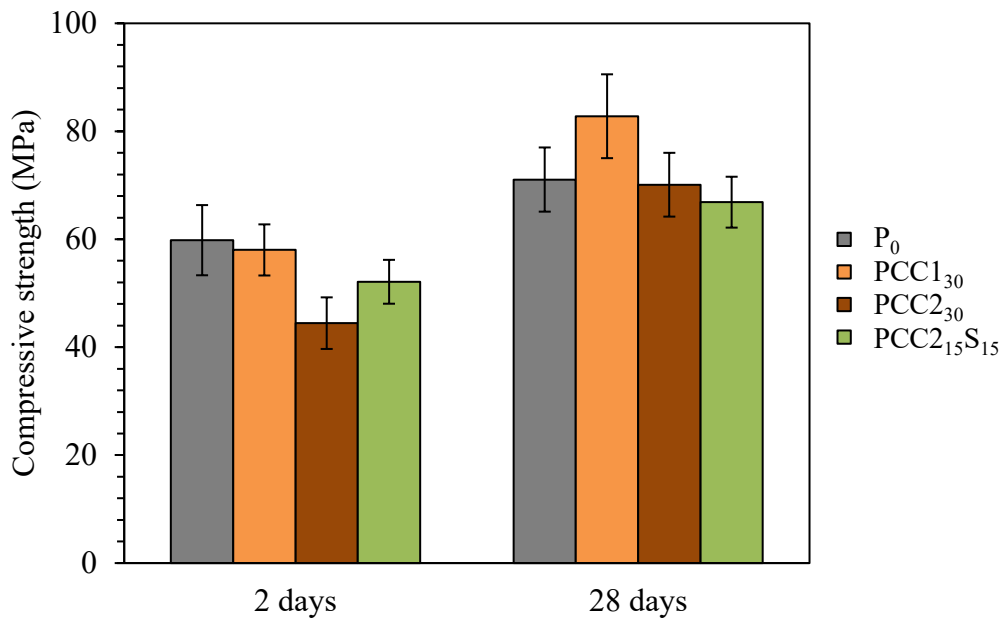


Fig. 3. Compressive strength of the cement paste mix designs at 2 and 28 days

277

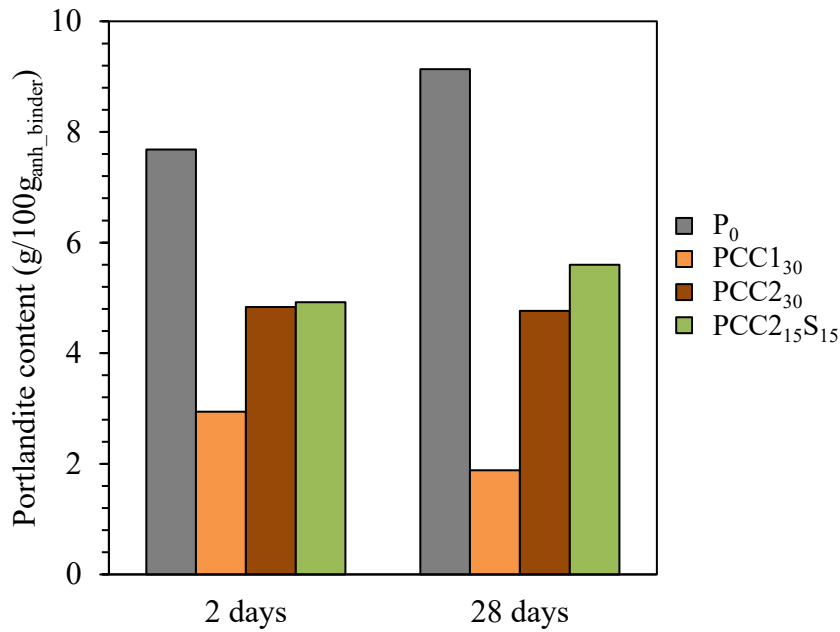
278

279

280 3.2 Microstructure investigation

281 3.2.1 Pozzolanic activity

282 Portlandite content was accurately quantified by means of thermogravimetric analysis as shown in
 283 Fig. 4. First of all, it can be noticed that the P₀ mixture showed the highest portlandite content at early
 284 and mature ages, whereas it was lower in PCC₁₃₀, PCC₂₃₀ and PCC₂₁₅S₁₅ due to clinker dilution
 285 effect and secondary hydration reactions. When comparing both binary binders, PCC₁₃₀ had a lower
 286 portlandite content which suggests that CC1 has a higher pozzolanic potential than CC2 leading to
 287 more portlandite consumption. The low portlandite content for PCC₁₃₀ at 2 days suggests that
 288 portlandite started being consumed at least at this point of hydration and thus that CC1 did already
 289 start reacting. The portlandite content continues to decrease until 28 days of hydration with CC1 use.
 290 Portlandite content do not seem to decrease in PCC₂₃₀ at 28 days, which can be a result of the filler
 291 effect of CC2 high quartz content, promoting further portlandite formation and compensating its
 292 consumption by pozzolanic reactivity. The ternary binder shows lower pozzolanicty compared to
 293 binary binders, suggesting the hydration of slag and more portlandite formation especially at 28 days.



294

295 **Fig. 4.** Portlandite content (per g of anhydrous binder) of the cement paste mix designs at 2 and 28
 296 days as determined by TGA

297

298 3.2.2 Pore structure

299 Fig. 5 displays the pore diameter distribution of each cement paste at both 2 and 28 days. It can be
 300 noticed that total porosity decreases from 2 to 28 days across all mixes, which is to be expected as
 301 hydration fills the pores. In addition, the pore structure changes significantly from 2 to 28 days in the
 302 cement blends, given the domination of pores with a diameter smaller than 0.01 μm at 28 days, as
 303 opposed to a diameter of between 0.01 and 0.1 μm at 2 days. This result was reported in [58] for
 304 metakaolin-incorporated pastes, and was explained by its pozzolanic reaction that results in higher
 305 amounts of CSH phase.

306 It can also be noticed that the total porosity of binary blends is higher than that of the reference mix,
 307 especially at early age. However, the quantity of pores with a diameter of between 0.01 and 0.1 μm
 308 is considerably reduced in the binary mixes, especially at 28 days. Moreover, the similar pore
 309 structure of these binders is refined, potentially enhancing durability properties. It is interesting to
 310 note that the low-grade calcined clay blend is less porous than PCC1₃₀, especially at early age, most
 311 likely due to the presence of quartz, which has a crystalline phase of minor porosity. As for the ternary
 312 blend, it can be noticed that the amount of total porosity is comparable to that of the reference mix at
 313 2 and 28 days, yet the quantity of capillary pores is significantly reduced, especially at 28 days in the
 314 ternary binder, which could lead to enhanced durability properties, proving a good synergy between
 315 GBFS and CC2.

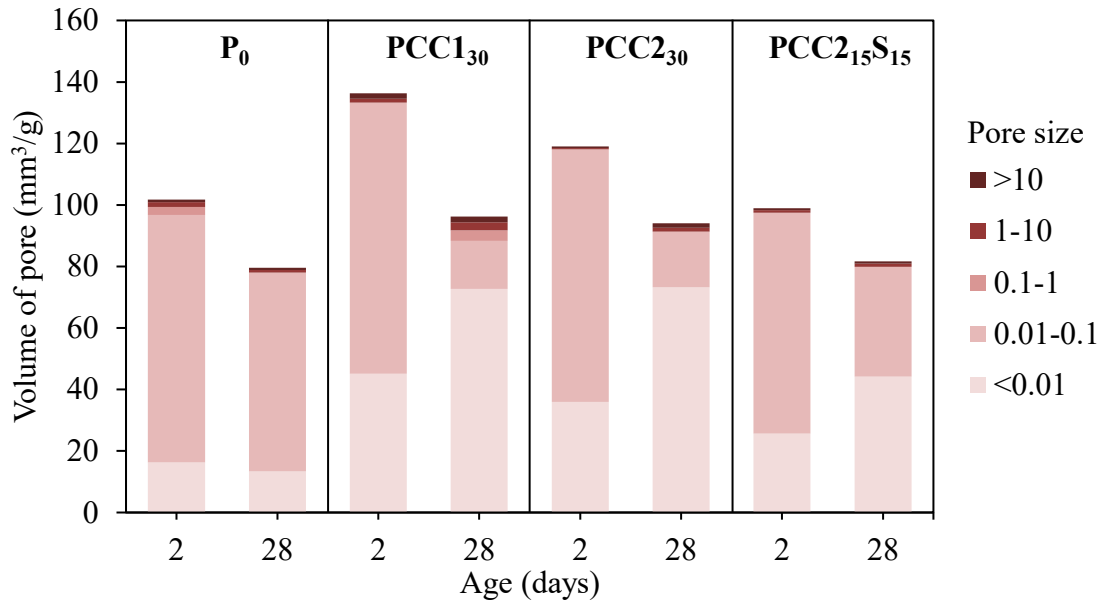


Fig. 5. Pore structure development for the cement pastes between 2 and 28 days (the pore size described is the pore diameter in μm and was limited to $100 \mu\text{m}$)

316
317
318

319

320 3.2.3 Microstructural analysis

321 The BSE micrographs of binary and ternary calcined clay systems at 2 and 28 days are shown in Fig.
322 6, as a means of comparing their microstructures. The main phases were annotated in the last image
323 to indicate the greyscale level of each phase and make the BSE images easier to read. For all mixes,
324 it is clear that the amount of unhydrated particles decreases from 2 to 28 days due to the hydration
325 process.

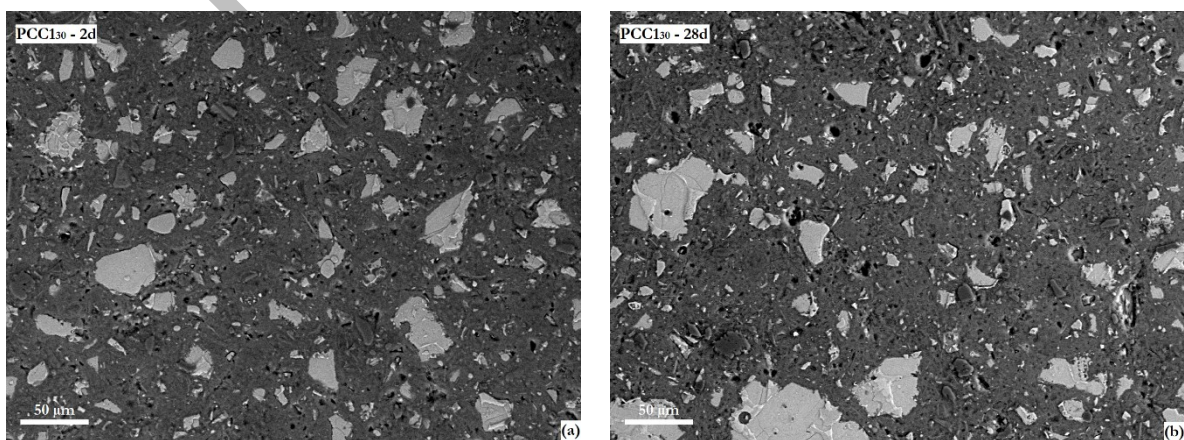
326 Figs. 6a and 6b show SEM images of CC1-binary binder respectively at 2 and 28 days, where few
327 visible calcined clay particles are observed (some small darker particles); which suggests its good
328 reactivity, especially at 28 days. No apparent microcrack-type defects are observed, explaining the
329 high compressive strength measured on this paste.

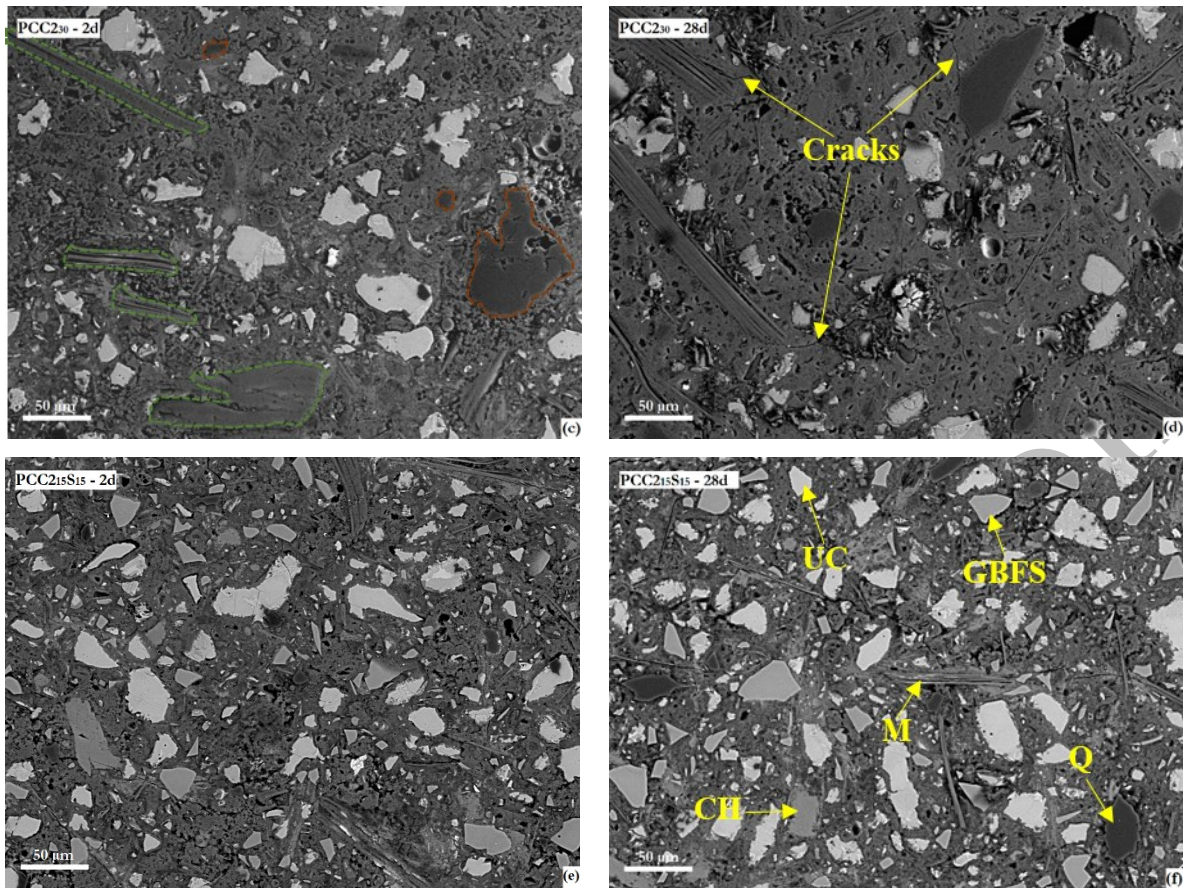
330 In comparison of PCC₁₃₀, PCC₂₃₀ shows smaller amounts of unhydrated cement particles at 2 and 28
331 days. Knowing that both binary pastes have the same amount of cement, we can conclude that PCC₂₃₀
332 has a higher degree of reaction of clinker at both ages. PCC₂₃₀ has also higher amounts of the dark
333 particles, in addition to some needle-shaped ones, circled respectively in brown and green dashed
334 lines in Fig. 6c, which are probably calcined clay particles, suggesting the lower reactivity of CC2
335 compared to CC1. In addition, some microcracks pointed in Fig. 6d appear at the edges of these
336 particles, which suggests a poor interface and weakening of the paste by these particles of impure
337 calcined clay.

338 To precisely assess the nature of the dark and needle-shaped particles, further EDS analyses were
339 carried out at the location of the same marked image (Fig. 6c) in order to obtain the aluminum,
340 calcium, silicon and potassium maps, as depicted respectively in the images of Fig. 7. All these
341 particles show no calcium traces, which confirms they are calcined clay phases. The elemental maps
342 show a strong correlation between Al and K locations, with small amounts of Si, which match with
343 the needle-shaped particles; this indicates that these are muscovite particles. The darkest particles
344 (e.g. the one marked in brown) belong to quartz, given that only Si can be detected in their location
345 using EDS. The existence of these calcined clay impurities prevents cement grains from being
346 uniformly dispersed in the cement matrix, thus causing reduced resistance, yet accompanied by
347 improved porosity, as explained above. Compared to PCC1₃₀, CC2-binary binder shows higher
348 amounts of calcined clays impurities (mainly quartz and muscovite) which is consistent with the XRD
349 quantification of both calcined clays. Besides, more portlandite is noticeable in the SEM images of
350 PCC2₃₀, which is consistent with TGA results.

351 Micrographs from the ternary mix (Figs. 6e and 6f) reveal a more heterogeneous cement paste with
352 the presence of both slag and CC2. Slag particles have sharper angles and are less lightly colored than
353 the unhydrated cement grains as annotated in the Fig. 6f. Compared to binary cement pastes, this
354 formulation shows a clear decrease in porosity. Compared to PCC2₃₀, the amount of residual
355 unhydrated particles at both ages is greater, but with higher portlandite amount that can be observed
356 on the SEM images and quantified by TGA. This suggests a probable hydration of some slag grains
357 promoted by CC2 filler effect (synergistic effect of both additions). In addition, the different
358 unhydrated cement and slag particles are well distributed in the cement paste, without apparent
359 decohesion or visible cracks, which may explain the paste's good macromechanical property.

360



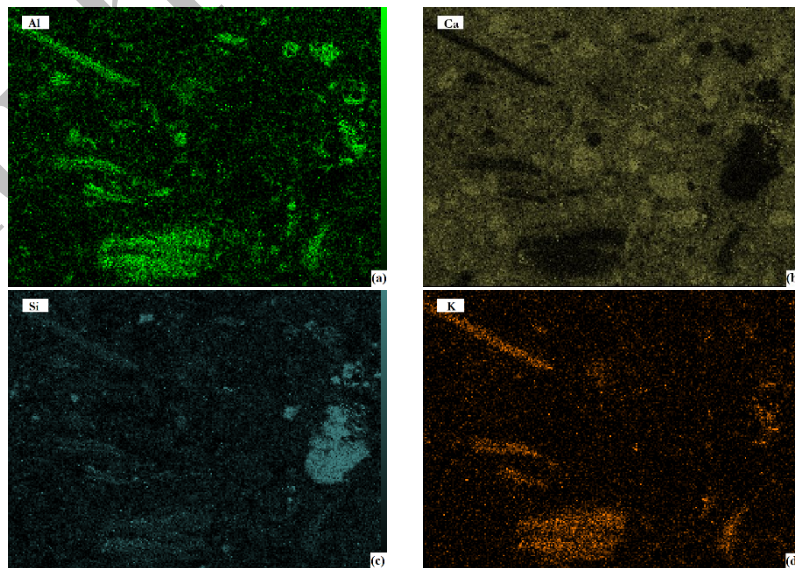


361 **Fig. 6.** SEM images of blended cement pastes: (a) PCC₁₃₀ at 2 days,
 362 (b) PCC₁₃₀ at 28 days, (c) PCC₂₃₀ at 2 days, (d) PCC₂₃₀ at 28 days, (e) PCC_{215S15} at 2 days and (f)
 363 PCC_{215S15} at 28 days. Brown dashed lines show quartz particles, and green ones show muscovite

364

365

366

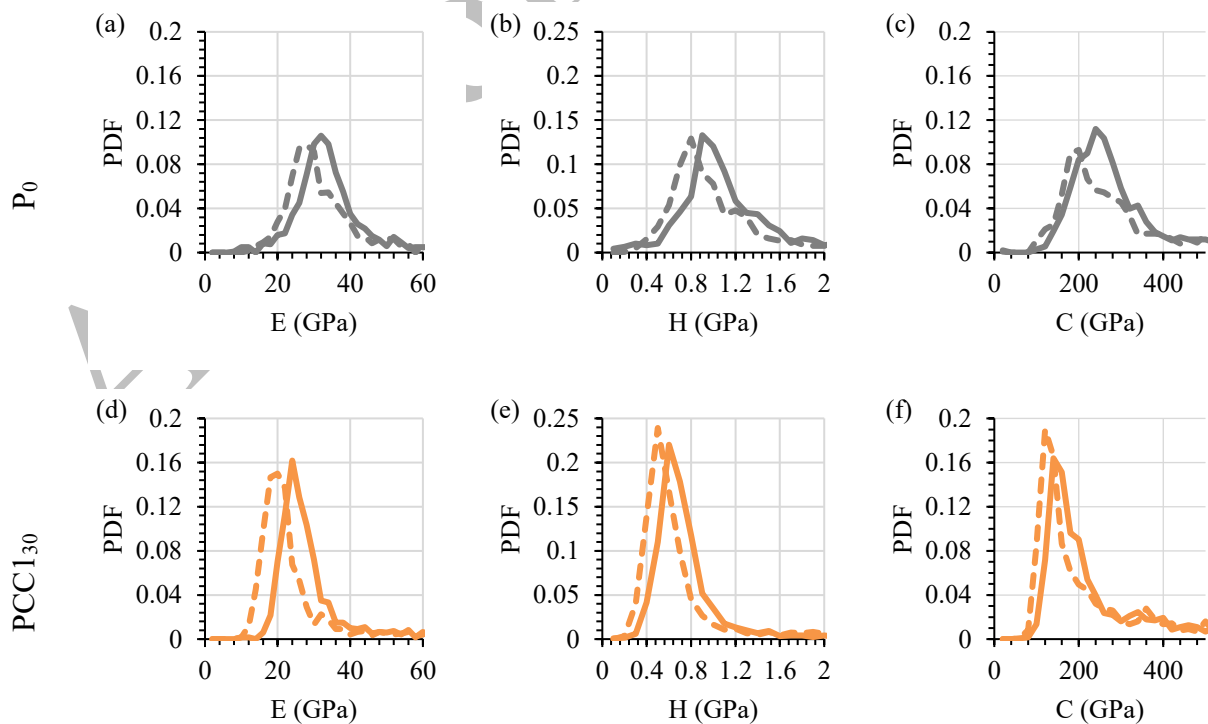


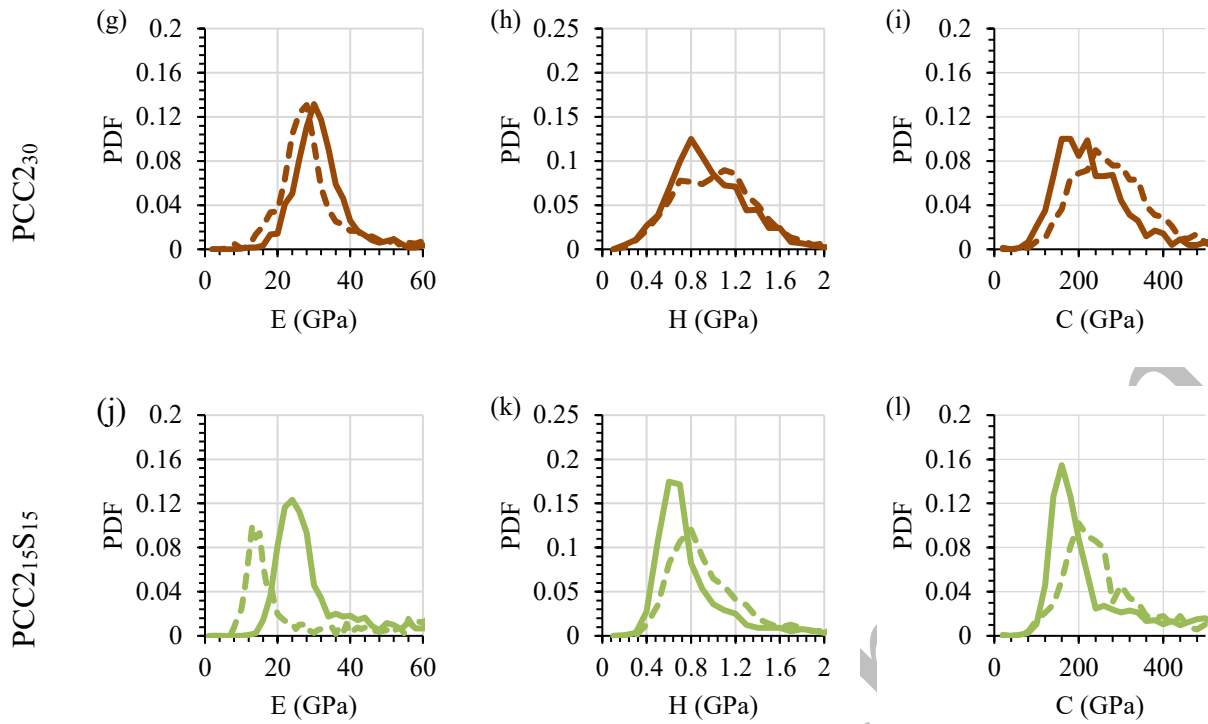
367 **Fig. 7.** SEM/EDS elemental maps of PCC₂₃₀ at 2 days (Fig. 6c) for (a) aluminium, (b) calcium,
 368 (c) silicon and (d) potassium

370 3.2.4 Micromechanical properties of the cement blends

371 Elastic properties were investigated at the microscale by means of nanoindentation. Figs. 8a-d-g-j
 372 show the probability density function in the elastic modulus for the four cement pastes at both 2 and
 373 28 days. Only the elastic moduli less than 60 GPa were depicted for analyzing hydration products'
 374 properties. From the outset, a shift can be observed towards higher values of elastic modulus from 2
 375 to 28 days across all mixes since the matrix stiffens with time of hydration. This shift equals 84.6%
 376 of the value at 2 days for the ternary binder and is much higher compared to the other cement pastes,
 377 reaching 14.3%, 20% and 7.1% respectively for P₀, PCC1₃₀ and PCC2₃₀. To explain this rate of
 378 microstructural development, the results of statistical deconvolution will be further presented and
 379 analyzed. The main peaks of hydration products at 2 and 28 days seem higher and narrower in PCC1₃₀
 380 which suggests a mono-phase predominance of a hydration product (CSH), and which is consistent
 381 with the small amount of portlandite found in PCC1₃₀ determined by TGA. The larger distributions
 382 in the other cement pastes indicate the presence of multiple hydration products with a higher content
 383 of the phase with properties towards the peak.

384 Likewise, the probability density functions of the hydrates' hardness are shown in Figs. 8b-e-h-k.
 385 Unlike elastic modulus, there is a shift towards decreasing hardness from 2 to 28 days in CC2 blended
 386 cement pastes (i.e. PCC2₃₀ and PCC2₁₅S₁₅).





387 **Fig. 8.** Probability density functions from statistical nanoindentation of (a-d-g-j) elastic modulus
 388 (bin size = 2 GPa), (b-e-h-k) hardness (bin size = 0.1 GPa) and (c-f-i-l) contact creep modulus
 389 (bin size = 20 GPa), for the different formulations at 2 and 28 days. Dashed and continuous lines
 390 are respectively for 2 and 28 days analysis

391

392 Fig. 9 shows the volumetric composition of each cement paste, and the details of deconvolution are
 393 summarized in Appendix A (tables A1 and A2 present the micromechanical properties of the clusters
 394 issued from statistical deconvolution for 1200 indents probed in the four cement pastes at 2 and 28
 395 days, and Fig A1 allows the visualization of the indents repartition in the two dimensions space
 396 composed of elastic modulus and hardness). For P_0 , four pure clusters could be detected and attributed
 397 as HD CSH, portlandite, interfaces between hydrates and unhydrated particles and finally unhydrated
 398 cement grains. The properties from the indents on interfaces can change depending on the amount of
 399 different phases in contact with the tip, and thus the standard deviations of these properties are high.
 400 Only HD CSH could be detected as the paste's w/b ratio is low, and its amount is higher from 2 to
 401 28 days, while it decreases for the unhydrated cement grains as shown in Fig. 9. It is worth noting
 402 that CSH can exist in two forms: low-density LD and high-density HD depending on the initial mix
 403 proportions of the pastes (mainly water-to-cement ratio, existence of chemical admixtures, mineral
 404 additions incorporations). Thus, these two forms have different micromechanical properties, lower
 405 for LD CSH, as widely proved in the literature [36].

406 In the cement blends, this same figure (Fig. 9) shows that the amount of unhydrated cement grains is
407 reduced due to the replacement of Portland cement with mineral additions, and different clusters with
408 more or less pure phases could be detected.

409 According to Fig. 9, the incorporation of 30% of CC1 resulted in 79% of CSH, higher than the
410 reference mix, with a high amount of LD CSH at 2 days and smaller one for HD CSH. The third
411 cluster was found to belong to both portlandite and interfaces as the amount of portlandite in this
412 paste is low. Then a last cluster that seems to be mainly for unhydrated cement grains but mixed with
413 some quartz particles brought by CC1, due to the slightly decreased mean properties along with higher
414 standard deviation of the properties compared to unhydrated particles properties from P₀. At 28 days,
415 more intermixed phases are detected as clusters, where it seems that there is a higher amount of HD
416 CSH compared to 2 days, probably due to the pozzolanic reaction of CC1.

417 Besides HD CSH, new clusters appeared in PCC2₃₀ at 2 days composed of CC2 most important
418 impurities, namely muscovite and quartz, which could be clearly identified in SEM images of PCC2₃₀
419 shown in Fig. 6. The second cluster was attributed to mixed portlandite and muscovite due to slightly
420 higher mean properties and standard deviation compared to portlandite in P₀. The average properties
421 of the third cluster seem to correspond to only quartz as the standard deviation of the properties is not
422 high, and the fourth one seems to belong to unhydrated cement grains but also to some interfaces
423 because the values of the properties are lower and more dispersed. At 28 days, only three clusters
424 could be detected among which there is HD CSH with higher amount than at 2 days. The higher
425 proportion of CSH observed in both binary binders in comparison with the reference mix is in
426 accordance with the higher fraction of gel pores observed using mercury porosity.

427 Finally, the ternary binder had clearly a slower reaction at 2 days with still a relatively high amount
428 of unhydrated cement particles (14.3%) and detected unhydrated slag grains. This agrees with the
429 images of PCC2₁₅S₁₅ microstructure shown in Figs. 5e and 5f where it visually appears that the paste
430 has higher amounts of unhydrated particles compared to the binary binders. Some portlandite was
431 also found to be mixed with HD CSH. At 28 days, it was hard to differentiate clusters with pure
432 phases due to the high heterogeneity of the cement paste, but it was naturally found to be a mixture
433 of LD and HD CSH, portlandite and unhydrated cement and slag particles.

434

435

436

437

438

439

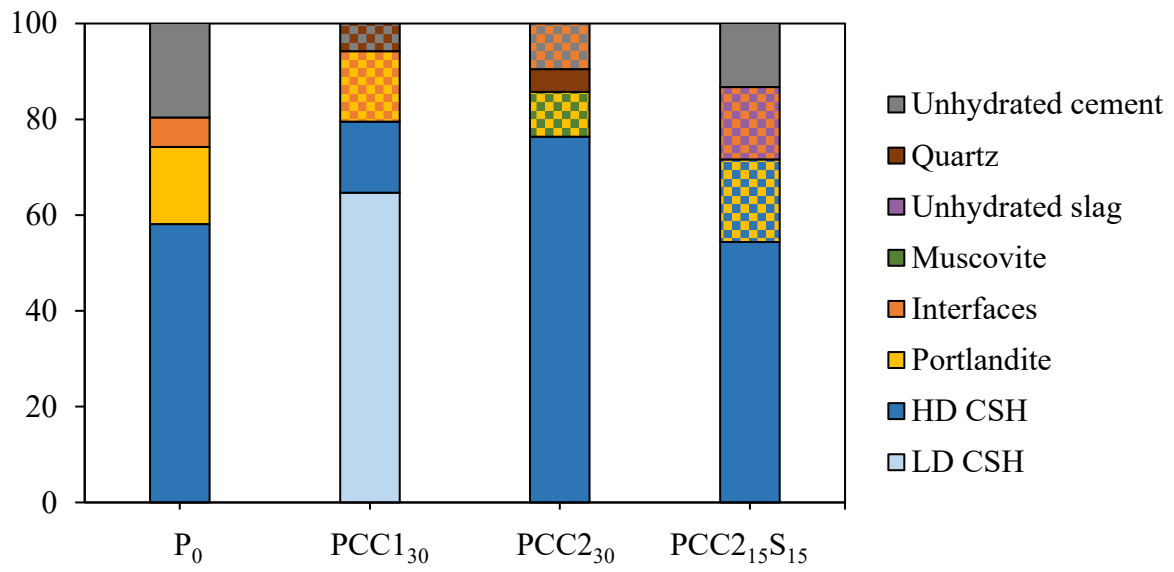
440

441

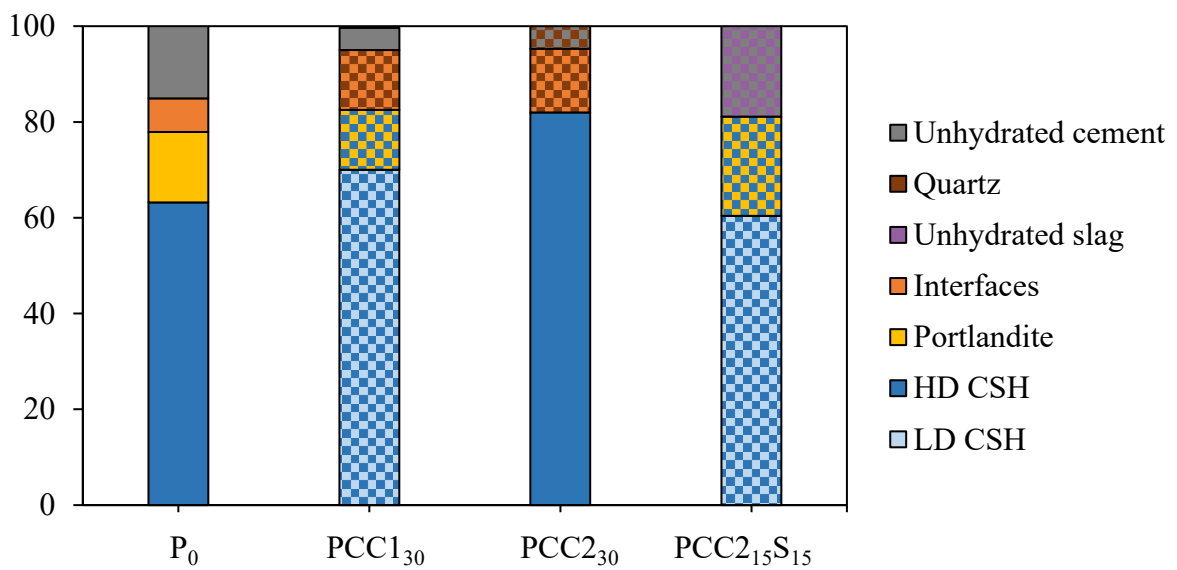
442



(a)



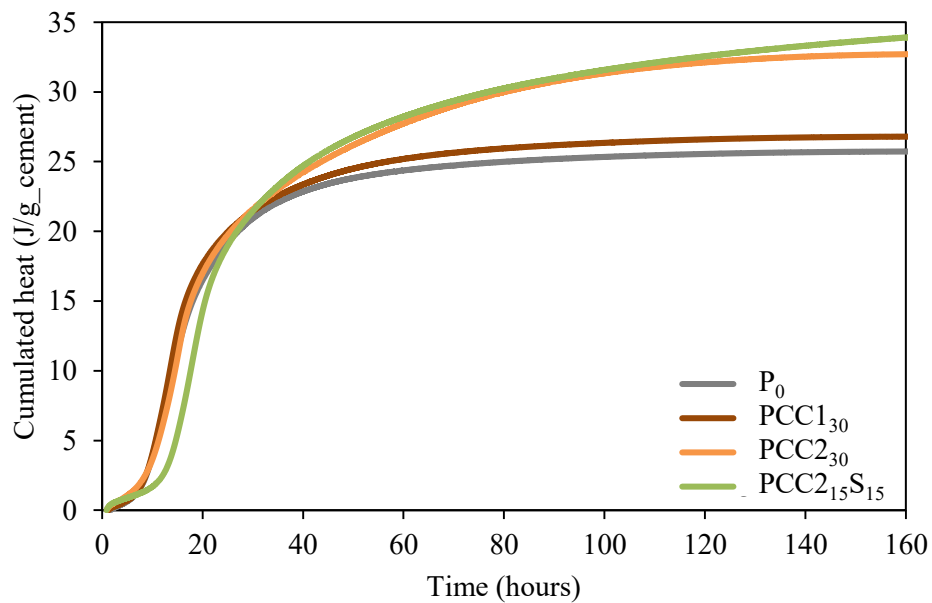
(b)



443 **Fig. 9.** Cement pastes compositions according to nanoindentation deconvolution results at
 444 (a) 2 days and (b) 28 days. Two-tone clusters (with two colours) indicate the existence of two
 445 phases in the same cluster according to the legend

446

447 In order to understand the cause of low-density phase dominance in PCC1₃₀ compared to the other
 448 mixes, calorimetric tests were run according to ASTM C1679-08 standard, and the results are
 449 depicted in Fig. 10. It can be seen that PCC1₃₀ exhibits much higher cumulative heat by gram of
 450 cement compared to P₀ after 30 hours of hydration. Based on this observation plus the fact that a
 451 higher degree of reaction of clinker was observed by SEM in PCC2₃₀, as compared to PCC1₃₀, it can
 452 be concluded that CC1 is much more reactive than CC2 and moreover that the observed heat
 453 difference stems from the CC1 reaction; which is consistent with TGA results and is probably due to
 454 its higher amorphous content. Also, a greater amount of cement is hydrated in PCC2₃₀, a probable
 455 consequence of the filler effect. This suggests that the hydration of calcined clay is the main cause of
 456 low-density CSH formation inside the cement paste.



457

458 **Fig. 10.** Normalized cumulative heat (per gram of cement) as obtained by calorimetry

459

460 3.2.5 Viscoelastic properties

461 3.2.5.1 General distribution of creep in the cement pastes

462 Figs. 8c-f-i-l show the probability density plots of the contact creep modulus for all four mix designs
 463 at both early (2 days) and advanced ages (28 days). These plots were limited to 500 GPa so as to
 464 compare the hydrates since they account for the predominant creep behavior in cementitious
 465 materials. The 2- to 28-day trend changes from one mix design to the next.

466 For CC2-based pastes, the mean contact creep modulus equals 200 GPa and 240 GPa for PCC2₁₅S₁₅
467 and PCC2₃₀ at 2 days, which proves to be respectively equivalent and 20% higher than the reference
468 mix. These mean values are consistent with HD CSH creep moduli according to [49]. Interestingly,
469 these two binders can be used for their strong creep resistance at an early age, with similar or even
470 better properties than CEM I paste albeit a smaller carbon footprint [1,59]. Then, a shift towards a
471 lower contact creep modulus can be observed from 2 to 28 days, which means that these pastes
472 develop good creep resistance at an early age, in decreasing with hydration, a finding that can be
473 explained by the formation of porous hydrates with limited creep properties, which was noticed in
474 mercury porosity results (i.e. the total porosity of these pastes remains relatively unchanged, despite
475 being much finer and containing a larger amount of gel pores).

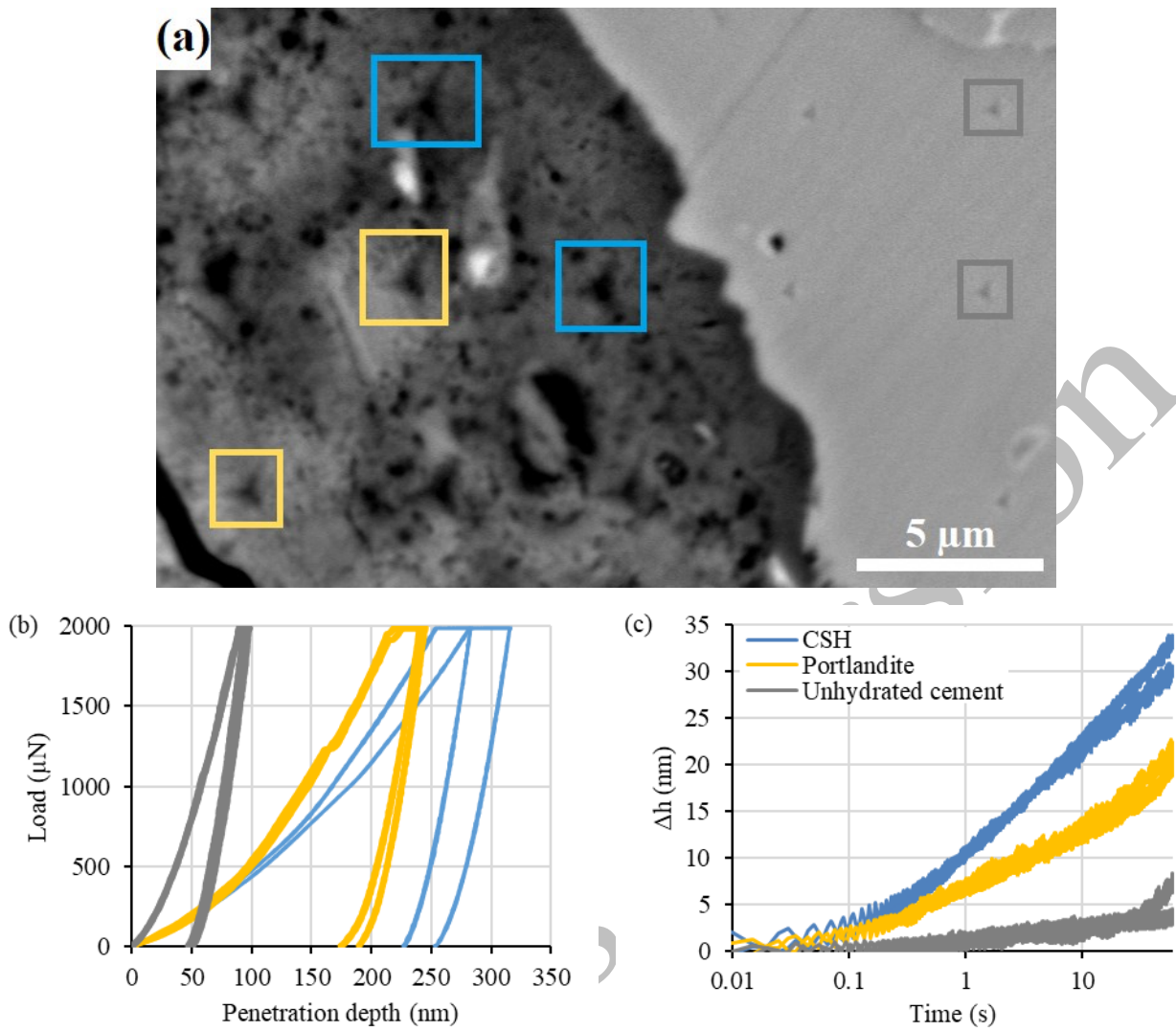
476 As for P₀ and PCC1₃₀, an increase in the contact creep modulus can be noticed from 2 to 28 days. The
477 contact creep modulus of PCC1₃₀ at the peak was 40% and 38.5% lower than P₀ resp. at 2 and 28 days.
478 This indicates a predominance of LD CSH in PCC1₃₀, with the formation of some HD CSH at
479 28 days. These observations are in accordance with calculated proportions of individual phases
480 (shown in Fig. 9) and mercury porosity results, and can be explained by combined calorimetry and
481 SEM results where CC1 was found to be with a high reactivity with lower clinker hydration rate.

482 3.2.5.2 Creep of individual phases

483 Fig. 11a shows a portion of indented area (a grid of 5 by 3 indents) in P₀ at 28 days where the imprints
484 of the 2 mN – indents are visible. Two indents from each phase were selected and their load-
485 penetration depth curves and logarithmic penetration depth change with time are shown in Figs. 11b
486 and 11c respectively. The selected indents were boxed in blue, gold and grey to refer to CSH,
487 portlandite and unhydrated cement respectively, identified on the basis of greyscale analysis of the
488 image. It can be noticed visually on the image that the size of imprints in the hydration products is
489 higher than that in unhydrated cement. This difference of size is less visible among indents in CSH
490 and portlandite. This observation is translated in the load-penetration depth curves with smaller
491 maximum penetration depth of indents in unhydrated cement, then in portlandite and CSH.

492 As for creep properties, it can be noticed that CSH has the highest deformation with a recorded depth
493 change of 31.8 ± 2.6 nm in 60 s creep. Meanwhile, the recorded depth change in portlandite on the
494 two indents is of 20.6 ± 1.0 nm, which represents 65% of that of CSH, commonly considered to be
495 responsible of concrete creep. This means that amount of portlandite in the hydration products and
496 its creep should be taken into account when analyzing the concrete behavior when subjected to creep.

497

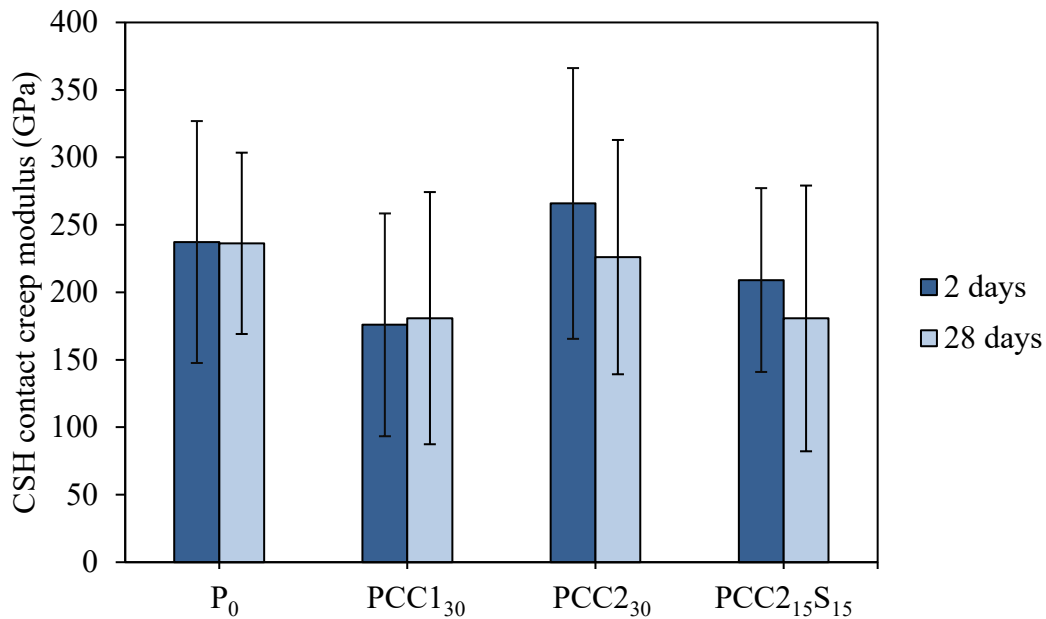


498 **Fig. 11.** (a) SEM image of indented area on P₀ at 28 days. Example of (b) load-penetration depth
 499 curves and (c) logarithmic penetration depth change vs. time of CSH, portlandite and unhydrated
 500 cement of the boxed indents

501

502 As explained in paragraph 2.2.6, contact creep modulus for CSH phase was calculated for all the
 503 mixes at 2 and 28 days. A mean value was taken into account when two types of CSH were found for
 504 one mix, and results are shown in Fig. 12. It can be noticed that all the calculated creep properties are
 505 within a range of 175 to 266 GPa which corresponds to the values reported in the literature for CSH
 506 phases. Some standard deviation values are high; this can be due to existence of some indents of
 507 portlandite in CSH-considered cluster, which are of higher contact creep modulus. It can also be
 508 noticed that PCC₁₃₀ creeps more than other formulations at 2 and 28 days, and this is because of the
 509 high amount of LD CSH detected in this mix design. As already noticed on the PDFs, the contact
 510 creep modulus tends to decrease in CC2-incorporated pastes, but in general, this property does not

511 vary significantly between 2 and 28 days. This means that the commonly observed trend of increased
512 creep with hydration time is mostly due to the higher fraction of CSH.



513

514

Fig. 12. CSH contact creep modulus for the four formulations at 2 and 28 days

515

516 4. Discussion

517 4.1 Impact of calcined clay composition on the cement paste properties

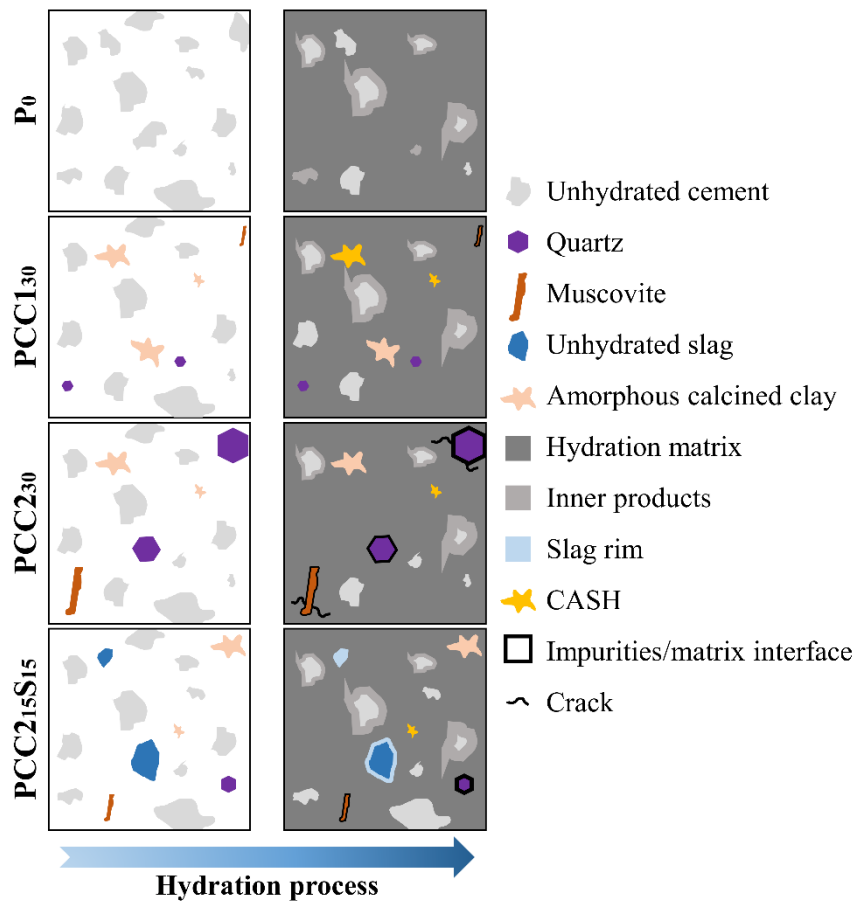
518 At the microscale, cement paste can be seen as a heterogeneous material of hard inclusions, which
519 are mainly the unhydrated cement grains, muscovite and quartz contributed by calcined clays and
520 embedded in a porous binding cement matrix constituted of softer hydrated phases, as shown in Fig.
521 13. Besides promoting the hydration capability of the unhydrated binder, the distribution of hard
522 particles in the hydrate matrix can influence the behavior of cement paste specimens regarding
523 compressive strength. Cementitious materials failure starts with the propagation of microcracks and
524 extends to the formation of major cracks; the existence of tough inclusions in cement pastes results
525 in greater toughness and crack inhibition [60].

526 At an age of 2 days, the microstructural investigation has shown that PCC₁₃₀ most important
527 hydration product is LD CSH which resulted in a higher porosity of the blend. Despite its high
528 reactivity at early age proved by combined TGA, SEM and calorimetry, high-grade calcined clay
529 resulted in low-density hydration products, which caused a deterioration of micromechanical
530 properties. However, PCC₁₃₀ does develop a higher compressive strength than PCC₂₃₀. This outcome
531 can be explained by the nature of the interface between the hydrate matrix and the hard inclusions: a

532 smooth transmission of some microcracks to hard particles can prevent their transformation into
533 macrocracks. Indeed, the system of hard inclusions in PCC1₃₀ is mainly composed of pure
534 constituents of Portland cement clinker, while PCC2₃₀ also contains a sizable amount of quartz and
535 muscovite contributed by CC2, which appear to cause some microcracks on the SEM images. The
536 nature of connection between these two distinct types of hard particles and cement matrices differs,
537 since quartz and muscovite do not participate in the hydration process, while the latter starts from
538 unhydrated cement particles and proceeds as a continuous process over time, which is illustrated in
539 Fig. 13. This finding is consistent with the results presented in [61], wherein the authors observed a
540 high compressive strength even at a 60% replacement rate of natural pozzolan (NP, slowly reactive),
541 which was explained by the optimal distribution of NP and cement grains from an incomplete reaction
542 in the mix.

543 At 28 days, this same behavior is still observed, although it is slightly reduced at the microstructural
544 scale as the hydration process continues over time. It becomes more effective in PCC1₃₀ since CC1
545 has greater amorphous content, as proven by a higher cumulative heat observed at 7 days, with a
546 stable outlook over the subsequent days of hydration. This explanation is also supported by the SEM
547 images of the microstructure, where it is shown that PCC1₃₀ has a uniform distribution of unhydrated
548 cement particles, with no visible microcracks, compared to PCC2₃₀, exhibiting fewer cement
549 inclusions and highly distinct quartz and muscovite particles.

550 The viscoelastic properties of calcined clay-based mixes tend to differ considerably at early age.
551 PCC1₃₀ tends to display a LD CSH-predominant microstructure with a small overlapping peak of
552 HD CSH, while PCC2₃₀ has a wide distribution that seems to cover the ranges of LD CSH and more
553 of HD CSH. In practice, creep can be both beneficial and harmful depending on the main goal of the
554 material used. A high creep resistance at early age can be beneficial for the prefabrication of large
555 structural elements subjected to their own weight that were unable to gain a sufficient level of
556 resistance. On the other hand, lower creep resistance enables a relaxation of stresses inside the
557 concrete matrix, as caused by temperature variation and shrinkage [62], thus lowering the risk of
558 cracking especially at an early age.



559
560 **Fig. 13.** Schematic representation of the cement pastes microstructures
561

562 **4.2 Synergistic effect of low-grade calcined clay and slag**

563 An interesting synergistic effect between low-grade calcined clay and slag was observed at multiple
564 scales. At the engineering scale, the compressive strength of PCC2₁₅S₁₅ is higher, relative to PCC₂₃₀
565 at early age. At 28 days, the values remained quite similar regarding the overlapping error bars. This
566 result is consistent with those of Khatib and Hibbert [63], or also Li *et al.* [19], who observed an
567 increase in compressive strength with both additions, as compared to a replacement with respectively
568 only slag or only metakaolin. Compared to a replacement with only low-grade calcined clay as
569 measured for PCC₂₃₀, or with only slag as studied by Gruyaert *et al.* [64], who show lower cumulative
570 heat for a paste with 30% replacement of slag with respect to ordinary Portland cement (w/b=0.5), a
571 higher heat release was shown at 7 days for the ternary binder, compared to both PCC₂₃₀ and P₀,
572 which tends to be higher at advanced ages, thereby confirming the underlying synergy.

573 At the microscale, a finer pore structure was observed with both additions, as well as a lower total
574 porosity at 2 and 28 days. This finding is in agreement with the results reported in [65], wherein a
575 reduced porosity was noticed for a mix replaced jointly by slag and metakaolin using MIP and

576 SEM - BSE in ultra-high performance concretes. Also, the ternary binder displayed faster stiffening
577 capability of the mix from 2 to 28 days, with respect to the other mixes.

578 **Conclusion and perspectives**

579 In this study, the utility of low-grade calcined clay in binary and ternary binders was highlighted
580 through a micromechanical study of cement pastes with 30% cement replacement at early (2 days)
581 and advanced (28 days) ages of hydration, supported by microstructural investigation in order to
582 explain macroscopic compressive strength. The main findings of this study can be summarized as
583 follows:

- 584 • Binary binder with low-grade calcined clay has 28 days-compressive strength equivalent to
585 ordinary Portland cement paste, results in finer pore structure with equivalent total porosity
586 with respect to ordinary Portland cement paste, all with lower hydration heat compared to
587 high-grade calcined clay
- 588 • High-grade calcined clay reacts faster and has higher pozzolanic activity compared to low-
589 grade one
- 590 • The fast reaction of high-grade calcined clay results in a higher gel porosity associated with
591 the formation of a low-density phase detected by nanoindentation especially at early age.
592 Therefore, low-grade calcined clay binary cement paste has better micromechanical
593 properties
- 594 • The mix proportions do not seem to influence the contact creep modulus of the pastes' CSH
- 595 • The calcined clay impurities (mainly quartz and muscovite) prevent good distribution of the
596 unhydrated cement particles and cause some microcracks, which influences the macroscale
597 compressive strength
- 598 • Ternary mix with both low-grade calcined clay and slag shows higher 2 days-compressive
599 strength compared to the substitution with only low-grade calcined clay, and has equivalent
600 28 days-compressive strength to Portland cement mix, with finer pore structure and slightly
601 lower total porosity

602 These results highlight the interest of mixing low-grade calcined clay with slag to enhance the
603 properties of binary mixes incorporating low-grade calcined clays. Similar performance could be
604 obtained with the same low-grade calcined clay, having a relatively high proportion of crystalline
605 phases, such as quartz, which has a filler effect during hydration, but whose large particles are prone
606 to create weaknesses favoring cracking.

607 Further tests on the nature of interfaces between hard inclusions and the hydrate matrix can be useful
608 in correlating micromechanical observations with the macroscale ones. In addition, classical
609 deconvolution processes should be combined to other techniques to better define clusters of single
610 pure phases.

611 **Acknowledgements**

612 The authors would like to acknowledge the raw materials examinations and tests performed by Vicat.

613

614

615

616

617

618

619

620

621

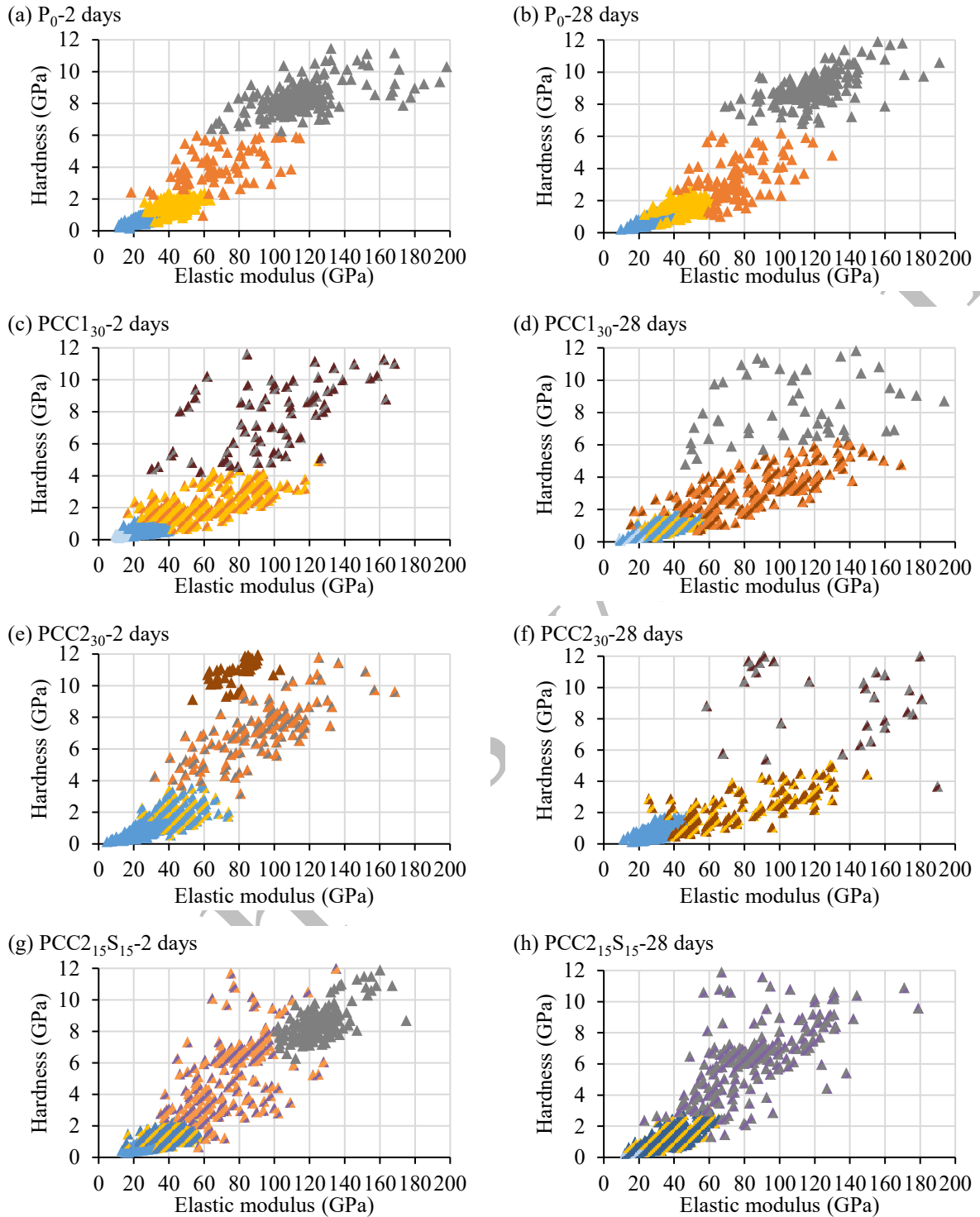
622

623

624

Authors' version

625 **Appendix A. Deconvolution results**



626 **Fig. A1.** Results of mechanical clustering using hardness vs. elastic modulus (light blue: LD CSH,
 627 dark blue: HD CSH, yellow: portlandite, orange: interfaces, green: muscovite, purple: unhydrated
 628 slag, brown: quartz and grey: unhydrated cement)

629
 630
 631

632 **Table A1**

633 Mean properties \pm standard deviation of the clusters resulting from the deconvolution of the four
 634 cement pastes and identification of the predominant phase(s) at 2 days.

Paste		1	2	3	4
P₀	E (GPa)	26.63 \pm 5.17	41.33 \pm 7.92	67.69 \pm 20.06	117.06 \pm 20.86
	H (GPa)	0.79 \pm 0.21	1.51 \pm 0.38	4.02 \pm 1.14	8.44 \pm 0.89
	Predominant phase	HD CSH	Portlandite	Interfaces	Unhydrated cement
PCC1₃₀	E (GPa)	18.30 \pm 3.13	27.72 \pm 5.24	64.12 \pm 23.14	99.22 \pm 31.91
	H (GPa)	0.47 \pm 0.12	0.76 \pm 0.25	2.38 \pm 0.92	7.74 \pm 2.09
	Predominant phase	LD CSH	HD CSH	Portlandite + interfaces	Unhydrated cement + Quartz
PCC2₃₀	E (GPa)	26.09 \pm 5.73	45.72 \pm 9.11	79.55 \pm 9.84	90.42 \pm 26.34
	H (GPa)	0.98 \pm 0.34	2.00 \pm 0.68	9.84 \pm 0.74	7.10 \pm 1.78
	Predominant phase	HD CSH	Portlandite + muscovite	Quartz	Unhydrated cement + Interfaces
PCC2₁₅S₁₅	E (GPa)	26.44 \pm 4.77	37.62 \pm 7.28	72.72 \pm 17.60	118.50 \pm 11.25
	H (GPa)	0.74 \pm 0.18	1.33 \pm 0.30	4.95 \pm 2.11	7.72 \pm 0.93
	Predominant phase	HD CSH	HD CSH + Portlandite	Interfaces + Unhydrated slag	Unhydrated cement

635

636

637

638

639

640

641

642 **Table A2**

643 Mean properties \pm standard deviation of the clusters resulting from the deconvolution of the four
 644 cement pastes and identification of the predominant phase(s) at 28 days.

Paste		1	2	3	4
P₀	E (GPa)	29.73 \pm 6.02	41.59 \pm 7.39	72.18 \pm 16.09	111.63 \pm 20.29
	H (GPa)	0.90 \pm 0.26	1.54 \pm 0.39	2.89 \pm 1.08	7.98 \pm 1.15
	Predominant phase	HD CSH	Portlandite	Interfaces	Unhydrated cement
PCC1₃₀	E (GPa)	23.90 \pm 3.72	37.47 \pm 7.50	87.77 \pm 30.85	109.84 \pm 38.88
	H (GPa)	0.60 \pm 0.14	0.99 \pm 0.32	3.34 \pm 1.19	8.14 \pm 1.92
	Predominant phase	LD CSH + HD CSH	HD CSH + Portlandite	Interfaces + Quartz	Unhydrated cement
PCC2₃₀	E (GPa)	29.50 \pm 5.60	78.03 \pm 29.82	120.16 \pm 40.23	
	H (GPa)	0.88 \pm 0.30	2.36 \pm 1.11	9.15 \pm 2.23	
	Predominant phase	HD CSH	Interfaces + Quartz	Unhydrated particles + Quartz	
PCC2₁₅S₁₅	E (GPa)	22.93 \pm 3.63	37.85 \pm 9.24	82.86 \pm 22.81	
	H (GPa)	0.60 \pm 0.14	1.36 \pm 0.58	6.49 \pm 2.50	
	Predominant phase	LD CSH + HD CSH	HD CSH + Portlandite	Interfaces + Quartz + Unhydrated slag and cement	

645

646 **References**

- 647 [1] K. Scrivener, F. Martirena, S. Bishnoi, S. Maity, Calcined clay limestone cements (LC3),
 648 Cement and Concrete Research. 114 (2018) 49–56.
 649 <https://doi.org/10.1016/j.cemconres.2017.08.017>.
- 650 [2] M. Murat, Hydration reaction and hardening of calcined clays and related minerals. I.
 651 Preliminary investigation on metakaolinite, Cement and Concrete Research. 13 (1983) 259–266.
 652 [https://doi.org/10.1016/0008-8846\(83\)90109-6](https://doi.org/10.1016/0008-8846(83)90109-6).
- 653 [3] G. Puerta-Falla, M. Balonis, G. Le Saout, N. Neithalath, G. Sant, The Influence of Metakaolin
 654 on Limestone Reactivity in Cementitious Materials, in: K. Scrivener, A. Favier (Eds.), Calcined
 655 Clays for Sustainable Concrete, Springer Netherlands, Dordrecht, 2015: pp. 11–19.
 656 https://doi.org/10.1007/978-94-017-9939-3_2.
- 657 [4] M. Boháč, M. Palou, R. Novotný, J. Másilko, D. Všianský, T. Staněk, Investigation on early
 658 hydration of ternary Portland cement-blast-furnace slag–metakaolin blends, Construction and
 659 Building Materials. 64 (2014) 333–341. <https://doi.org/10.1016/j.conbuildmat.2014.04.018>.
- 660 [5] E.-H. Kadri, S. Kenai, K. Ezziane, R. Siddique, G. De Schutter, Influence of metakaolin and
 661 silica fume on the heat of hydration and compressive strength development of mortar, Applied
 662 Clay Science. 53 (2011) 704–708. <https://doi.org/10.1016/j.clay.2011.06.008>.
- 663 [6] S. Wild, J.M. Khatib, Portlandite consumption in metakaolin cement pastes and mortars, Cement
 664 and Concrete Research. 27 (1997) 137–146. [https://doi.org/10.1016/S0008-8846\(96\)00187-1](https://doi.org/10.1016/S0008-8846(96)00187-1).
- 665 [7] F. Curcio, B.A. DeAngelis, S. Pagliolico, Metakaolin as a pozzolanic microfiller for high-
 666 performance mortars, Cement and Concrete Research. 28 (1998) 803–809.
 667 [https://doi.org/10.1016/S0008-8846\(98\)00045-3](https://doi.org/10.1016/S0008-8846(98)00045-3).
- 668 [8] M.A. Caldarone, K.A. Gruber, R.G. Burg, High Reactivity Metakaolin (HRM): A New
 669 Generation Mineral Admixture for High Performance Concrete, CI. 16 (1994) 37–41.
- 670 [9] X. Qian, Z. Li, The relationships between stress and strain for high-performance concrete with
 671 metakaolin, Cement and Concrete Research. 31 (2001) 1607–1611.
 672 [https://doi.org/10.1016/S0008-8846\(01\)00612-3](https://doi.org/10.1016/S0008-8846(01)00612-3).
- 673 [10] J. Ambroise, S. Maximilien, J. Pera, Properties of Metakaolin blended cements, Advanced
 674 Cement Based Materials. 1 (1994) 161–168. [https://doi.org/10.1016/1065-7355\(94\)90007-8](https://doi.org/10.1016/1065-7355(94)90007-8).
- 675 [11] V.N. Dwivedi, N.P. Singh, S.S. Das, N.B. Singh, A new pozzolanic material for cement
 676 industry: Bamboo leaf ash, Int. J. Phys. Sci. (n.d.) 6.
- 677 [12] B. Sabir, S. Wild, J. Bai, Metakaolin and calcined clays as pozzolans for concrete: a review,
 678 Cement and Concrete Composites. 23 (2001) 441–454. <https://doi.org/10/dscwv7>.
- 679 [13] A.H. Asbridge, G.A. Chadbourn, C.L. Page, Effects of metakaolin and the interfacial transition
 680 zone on the diffusion of chloride ions through cement mortars, Cement and Concrete Research.
 681 31 (2001) 1567–1572. [https://doi.org/10.1016/S0008-8846\(01\)00598-1](https://doi.org/10.1016/S0008-8846(01)00598-1).
- 682 [14] C. Girodet, M. Chabannet, J.L. Bosc, J. Pera, Influence of the type of cement on the freeze-thaw
 683 resistance of the mortar phase of concrete, in: London, 1997: pp. 31–40.
- 684 [15] B.B. Sabir, S. Wild, J.M. Khatib, On the Workability and Strength Development of MK
 685 Concrete, in: 1996: pp. 651–662.
- 686 [16] K. Scrivener, F. Avet, H. Maraghechi, F. Zunino, J. Ston, W. Hanpongpun, A. Favier, Impacting
 687 factors and properties of limestone calcined clay cements (LC3), Green Materials. 7 (2019) 3–
 688 14. <https://doi.org/10.1680/jgrma.18.00029>.
- 689 [17] A. Zolfagharnasab, A.A. Ramezani-pour, F. Bahman-Zadeh, Investigating the potential of
 690 low-grade calcined clays to produce durable LC3 binders against chloride ions attack,
 691 Construction and Building Materials. 303 (2021) 124541.
 692 <https://doi.org/10.1016/j.conbuildmat.2021.124541>.
- 693 [18] Q.D. Nguyen, T. Kim, A. Castel, Mitigation of alkali-silica reaction by limestone calcined clay
 694 cement (LC3), Cement and Concrete Research. 137 (2020) 106176.
 695 <https://doi.org/10.1016/j.cemconres.2020.106176>.

- 696 [19] Z. Li, Z. Ding, Property improvement of Portland cement by incorporating with metakaolin and
697 slag, *Cement and Concrete Research*. 33 (2003) 579–584. [https://doi.org/10.1016/S0008-8846\(02\)01025-6](https://doi.org/10.1016/S0008-8846(02)01025-6).
698
- 699 [20] F. Cassagnabère, M. Lachemi, M. Mouret, G. Escadeillas, Caractérisation performantielle d'un
700 liant ternaire à base de ciment, laitier et métakaolin, *Can. J. Civ. Eng.* 38 (2011) 837–848.
701 <https://doi.org/10.1139/111-043>.
- 702 [21] W. Chen, J. Dang, H. Du, Using low-grade calcined clay to develop low-carbon and lightweight
703 strain-hardening cement composites, *Journal of Building Engineering*. 58 (2022) 105023.
704 <https://doi.org/10.1016/j.jobe.2022.105023>.
- 705 [22] C.S. Malacarne, M.A. Longhi, M.R.C. Silva, J.P. Gonçalves, E.D. Rodríguez, A.P. Kirchheim,
706 Influence of low-grade materials as clinker substitute on the rheological behavior, hydration and
707 mechanical performance of ternary cements, *Case Studies in Construction Materials*. 15 (2021)
708 e00776. <https://doi.org/10.1016/j.cscm.2021.e00776>.
- 709 [23] S. Krishnan, D. Gopala Rao, S. Bishnoi, Why Low-Grade Calcined Clays Are the Ideal for the
710 Production of Limestone Calcined Clay Cement (LC3), in: S. Bishnoi (Ed.), *Calcined Clays for
711 Sustainable Concrete*, Springer, Singapore, 2020: pp. 125–130. https://doi.org/10.1007/978-981-15-2806-4_14.
712
- 713 [24] G. Cardinaud, E. Rozière, O. Martinage, A. Loukili, L. Barnes-Davin, M. Paris, D. Deneele,
714 Calcined clay – Limestone cements: Hydration processes with high and low-grade kaolinite
715 clays, *Construction and Building Materials*. 277 (2021) 122271.
716 <https://doi.org/10.1016/j.conbuildmat.2021.122271>.
- 717 [25] Y. Chen, C. Romero Rodriguez, Z. Li, B. Chen, O. Çopuroğlu, E. Schlangen, Effect of different
718 grade levels of calcined clays on fresh and hardened properties of ternary-blended cementitious
719 materials for 3D printing, *Cement and Concrete Composites*. 114 (2020) 103708.
720 <https://doi.org/10.1016/j.cemconcomp.2020.103708>.
- 721 [26] C. Hu, Z. Li, A review on the mechanical properties of cement-based materials measured by
722 nanoindentation, *Construction and Building Materials*. 90 (2015) 80–90.
723 <https://doi.org/10/gd8436>.
- 724 [27] G. Fang, Q. Wang, M. Zhang, Micromechanical analysis of interfacial transition zone in alkali-
725 activated fly ash-slag concrete, *Cement and Concrete Composites*. (2021) 103990.
726 <https://doi.org/10.1016/j.cemconcomp.2021.103990>.
- 727 [28] D. Damidot, K. Velez, F. Sorrentino, Characterization of Interstitial Transition Zone (ITZ) of
728 High Performance Cement by Nanoindentation Technique, *Proceedings of the 11th International
729 Congress on the Chemistry of Cement*,. (2003) 11.
- 730 [29] S. Liu, P. Shen, D. Xuan, L. Li, A. Sojobi, B. Zhan, C.S. Poon, A comparison of liquid-solid
731 and gas-solid accelerated carbonation for enhancement of recycled concrete aggregate, *Cement
732 and Concrete Composites*. 118 (2021) 103988.
733 <https://doi.org/10.1016/j.cemconcomp.2021.103988>.
- 734 [30] B. Hilloulin, M. Lagrange, M. Duvillard, G. Garioud, ϵ -greedy automated indentation of
735 cementitious materials for phase mechanical properties determination, *Cement and Concrete
736 Composites*. 129 (2022) 104465. <https://doi.org/10.1016/j.cemconcomp.2022.104465>.
- 737 [31] B. Hilloulin, M. Robira, A. Loukili, Coupling statistical indentation and microscopy to evaluate
738 micromechanical properties of materials: Application to viscoelastic behavior of irradiated
739 mortars, *Cement and Concrete Composites*. 94 (2018) 153–165. <https://doi.org/10/ghdf49>.
- 740 [32] Z. Luo, W. Li, Y. Gan, K. Mendu, S.P. Shah, Applying grid nanoindentation and maximum
741 likelihood estimation for N-A-S-H gel in geopolymers paste: Investigation and discussion,
742 *Cement and Concrete Research*. 135 (2020) 106112.
743 <https://doi.org/10.1016/j.cemconres.2020.106112>.
- 744 [33] J. Ying, X. Zhang, Z. Jiang, Y. Huang, On Phase Identification of Hardened Cement Pastes by
745 Combined Nanoindentation and Mercury Intrusion Method, *Materials*. 14 (2021) 3349.
746 <https://doi.org/10.3390/ma14123349>.

- 747 [34] G. Constantinides, F.-J. Ulm, K. Van Vliet, On the use of nanoindentation for cementitious
748 materials, *Mat. Struct.* 36 (2003) 191–196. <https://doi.org/10/ffkbhj>.
- 749 [35] G. Constantinides, F.-J. Ulm, The nanogranular nature of C–S–H, *Journal of the Mechanics and*
750 *Physics of Solids.* 55 (2007) 64–90. <https://doi.org/10.1016/j.jmps.2006.06.003>.
- 751 [36] M. Vandamme, F.-J. Ulm, P. Fonollosa, Nanogranular packing of C–S–H at substochiometric
752 conditions, *Cement and Concrete Research.* 40 (2010) 14–26. <https://doi.org/10/dgjn5t>.
- 753 [37] H. Chualin, L. Zongjin, Property investigation of individual phases in cementitious composites
754 containing silica fume and fly ash, *Cement and Concrete Composites.* 57 (2015) 17–26.
755 <https://doi.org/10.1016/j.cemconcomp.2014.11.011>.
- 756 [38] P. Mondal, S.P. Shah, L.D. Marks, J.J. Gaitero, Comparative Study of the Effects of Microsilica
757 and Nanosilica in Concrete, *Transportation Research Record.* 2141 (2010) 6–9.
758 <https://doi.org/10/cdzcj2>.
- 759 [39] S. Barbhuiya, P. Chow, S. Memon, Microstructure, hydration and nanomechanical properties of
760 concrete containing metakaolin, *Construction and Building Materials.* 95 (2015) 696–702.
761 <https://doi.org/10.1016/j.conbuildmat.2015.07.101>.
- 762 [40] C. Hu, Z. Li, Y. Gao, Y. Han, Y. Zhang, Investigation on microstructures of cementitious
763 composites incorporating slag, *Advances in Cement Research.* 26 (2014) 222–232.
- 764 [41] N. Shanahan, A. Markandeya, A. Elnihum, Y.P. Stetsko, A. Zayed, Multi-technique
765 investigation of metakaolin and slag blended portland cement pastes, *Applied Clay Science.*
766 132–133 (2016) 449–459. <https://doi.org/10.1016/j.clay.2016.07.015>.
- 767 [42] J. Li, Y. Yao, A study on creep and drying shrinkage of high performance concrete, *Cement and*
768 *Concrete Research.* 31 (2001) 1203–1206. [https://doi.org/10.1016/S0008-8846\(01\)00539-7](https://doi.org/10.1016/S0008-8846(01)00539-7).
- 769 [43] L. Charpin, Y. Le Pape, É. Coustabeau, É. Toppani, G. Heinfling, C. Le Bellego, B. Masson, J.
770 Montalvo, A. Courtois, J. Sanahuja, N. Reviron, A 12year EDF study of concrete creep under
771 uniaxial and biaxial loading, *Cement and Concrete Research.* 103 (2018) 140–159.
772 <https://doi.org/10.1016/j.cemconres.2017.10.009>.
- 773 [44] M. Vandamme, F.-J. Ulm, Nanogranular origin of concrete creep, *Proceedings of the National*
774 *Academy of Sciences.* 106 (2009) 10552–10557. <https://doi.org/10/dfs8nq>.
- 775 [45] C. Pichler, R. Lackner, Identification of Logarithmic-Type Creep of Calcium-Silicate-Hydrates
776 by Means of Nanoindentation, *Strain.* 45 (2009) 17–25. <https://doi.org/10/fc8wfn>.
- 777 [46] M. Vandamme, F.-J. Ulm, Nanoindentation investigation of creep properties of calcium silicate
778 hydrates, *Cement and Concrete Research.* 52 (2013) 38–52. <https://doi.org/10/f5f4zk>.
- 779 [47] M. Irfan-ul-Hassan, B. Pichler, R. Reihnsner, Ch. Hellmich, Elastic and creep properties of young
780 cement paste, as determined from hourly repeated minute-long quasi-static tests, *Cement and*
781 *Concrete Research.* 82 (2016) 36–49. <https://doi.org/10.1016/j.cemconres.2015.11.007>.
- 782 [48] Y. Wei, S. Liang, X. Gao, Indentation creep of cementitious materials: Experimental
783 investigation from nano to micro length scales, *Construction and Building Materials.* 143 (2017)
784 222–233. <https://doi.org/10.1016/j.conbuildmat.2017.03.126>.
- 785 [49] Y. Li, Y. Liu, Z. Wang, H. Li, J. Mu, Effect of phases on the creep properties of cement paste
786 based on indentation test and homogenization scheme, *Construction and Building Materials.*
787 317 (2022) 125957. <https://doi.org/10.1016/j.conbuildmat.2021.125957>.
- 788 [50] Y. Li, Y. Liu, Y. Li, Y. Li, R. Wang, Evaluation of concrete creep properties based on
789 indentation test and multiscale homogenization method, *Cement and Concrete Composites.*
790 (2021) 104135. <https://doi.org/10.1016/j.cemconcomp.2021.104135>.
- 791 [51] Y. Dhandapani, M. Santhanam, Assessment of pore structure evolution in the limestone calcined
792 clay cementitious system and its implications for performance, *Cement and Concrete*
793 *Composites.* 84 (2017) 36–47. <https://doi.org/10.1016/j.cemconcomp.2017.08.012>.
- 794 [52] K. Scrivener, R. Snellings, B. Lothenbach, *A practical guide to microstructural analysis*, 2015.
- 795 [53] B.K. Marsh, R.L. Day, Pozzolanic and cementitious reactions of fly ash in blended cement
796 pastes, *Cement and Concrete Research.* 18 (1988) 301–310. [https://doi.org/10.1016/0008-8846\(88\)90014-2](https://doi.org/10.1016/0008-8846(88)90014-2).
- 797

- 798 [54] W.C. Oliver, G.M. Pharr, An improved technique for determining hardness and elastic modulus
799 using load and displacement sensing indentation experiments, *Journal of Materials Research*. 7
800 (1992) 1564–1583. <https://doi.org/10/bdv47f>.
- 801 [55] G. Constantinides, F.-J. Ulm, The effect of two types of C-S-H on the elasticity of cement-based
802 materials: Results from nanoindentation and micromechanical modeling, *Cement and Concrete*
803 *Research*. 34 (2004) 67–80. [https://doi.org/10.1016/S0008-8846\(03\)00230-8](https://doi.org/10.1016/S0008-8846(03)00230-8).
- 804 [56] Z.-H. He, C.-X. Qian, Nanoindentation Characteristics of Cement with Metakaolin Under
805 Different Curing Systems, *Nanosci Nanotechnol Lett*. 6 (2014) 721–725.
806 <https://doi.org/10.1166/nnl.2014.1832>.
- 807 [57] Y. Liu, A. Liu, S. Liu, Y. Kang, Nano-scale mechanical properties of constituent minerals in
808 shales investigated by combined nanoindentation statistical analyses and SEM-EDS-XRD
809 techniques, *International Journal of Rock Mechanics and Mining Sciences*. 159 (2022) 105187.
810 <https://doi.org/10.1016/j.ijrmms.2022.105187>.
- 811 [58] M. Frías, J. Cabrera, Pore size distribution and degree of hydration of metakaolin–cement pastes,
812 *Cement and Concrete Research*. 30 (2000) 561–569. [https://doi.org/10.1016/S0008-8846\(00\)00203-9](https://doi.org/10.1016/S0008-8846(00)00203-9).
- 813 [59] IFPEB, Carbone 4, Brief-Filiere-Beton, France, 2020.
- 814 [60] J.H. Brown, C.D. Pomeroy, Fracture toughness of cement paste and mortars, *Cement and*
815 *Concrete Research*. 3 (1973) 475–480. [https://doi.org/10.1016/0008-8846\(73\)90085-9](https://doi.org/10.1016/0008-8846(73)90085-9).
- 816 [61] W. Wilson, J.M. Rivera-Torres, L. Sorelli, A. Durán-Herrera, A. Tagnit-Hamou, The
817 micromechanical signature of high-volume natural pozzolan concrete by combined statistical
818 nanoindentation and SEM-EDS analyses, *Cement and Concrete Research*. 91 (2017) 1–12.
819 <https://doi.org/10.1016/j.cemconres.2016.10.004>.
- 820 [62] P. Meshgin, K.-K. Choi, M.M. Reda Taha, Experimental and analytical investigations of creep
821 of epoxy adhesive at the concrete–FRP interfaces, *International Journal of Adhesion and*
822 *Adhesives*. 29 (2009) 56–66. <https://doi.org/10.1016/j.ijadhadh.2008.01.003>.
- 823 [63] J.M. Khatib, J.J. Hibbert, Selected engineering properties of concrete incorporating slag and
824 metakaolin, *Construction and Building Materials*. 19 (2005) 460–472.
825 <https://doi.org/10.1016/j.conbuildmat.2004.07.017>.
- 826 [64] E. Gruyaert, N. Robeyst, N. De Belie, Study of the hydration of Portland cement blended with
827 blast-furnace slag by calorimetry and thermogravimetry, *J Therm Anal Calorim*. 102 (2010)
828 941–951. <https://doi.org/10.1007/s10973-010-0841-6>.
- 829 [65] P. Zhan, J. Xu, J. Wang, C. Jiang, Multi-scale study on synergistic effect of cement replacement
830 by metakaolin and typical supplementary cementitious materials on properties of ultra-high
831 performance concrete, *Construction and Building Materials*. 307 (2021) 125082.
832 <https://doi.org/10.1016/j.conbuildmat.2021.125082>.
- 833
834